Modelling the Heat-transfer, Solidification and Associated Precipitation Kinetics during Continuous Slab Casting of Micro Alloyed Steels

Submitted in partial fulfilment of the requirements for the degree of Master of Technology

By

R. Seenivasan

Roll No. 163114005

Under the guidance of

Prof. N. N. Viswanathan

Prof. M. P. Gururajan

Steel Technology

Department of Metallurgical Engineering and Materials Science

INDIAN INSTITUTE OF TECHNOLOGY BOMBAY

2018

Dissertation Approval Sheet

The dissertation entitled "**Modelling the Heat-transfer, Solidification and Associated Precipitation Kinetics during Continuous Slab Casting of Micro Alloyed Steels**" submitted by **R. Seenivasan** (Roll No:163114005) is approved for the degree of Master of Technology in Steel Technology from Indian Institute of Technology, Bombay.

Date: 20 June 2018

_____
Project Guide

_____
Chairman

_____
Co-Guide

_____
External Examiner

_____
Internal Examiner

Declaration

I declare that this written submission represents my ideas in my own words and where others ideas or words have been included; I have adequately cited and referenced the original source. I also declare that I have adhered to all principles of academic honesty and integrity and have not misrepresented or fabricated or falsified any idea/data/fact/ source in my submission. I understand that any violation of the above will be cause for disciplinary action by the institute and can evoke penal action from the sources which have thus not been properly cited or from whom the proper submission has not been taken when needed.

_____

(Signature)

R. Seenivasan

163114005

Acknowledgement

I would like to take this opportunity to express a deep sense of gratitude to my guide, Prof. N. N. Viswanathan and my co-guide Prof. M. P. Gururajan for imparting their knowledge and for teaching me the art of research. Their continuous encouragement and competent guidance motivated me and instilled a sense of confidence in me. I am grateful to Prof. N. B. Ballal for the encouraging discussions and thoughtful suggestions given throughout this period. I also thank all other professors of Metallurgical Engineering and Material Science Department, Indian Institute of Technology, Bombay who have given their invaluable time in sharing their thoughts on various subjects.

I feel great pleasure on extending my heartfelt thanks to Mr. S. Manjini (Associate Vice president, Research and Development Department) to confer this area of work and JSW Steel Ltd, Bellary for providing the opportunity to study in this campus.

I am also grateful to my friends, Ms. Snigdha, Mr. Angshuman and Mr. Karundev, for their valuable time in helping me out various stages of my project.

Finally, I must mention the relentless support and endless sacrifices by my family for which I shall forever obliged.

R. Seenivasan

IITB, 20 June 2018

ABSTRACT

The aim of the work is to provide fundamental understanding of heat transfer, solidification and associated precipitation kinetics during continuous slab casting of micro alloyed steel. The one dimensional transient heat conduction by enthalpy method is developed to predict the thermal history and shell growth of the strand. The boundary conditions for mould, spray, air cooling and roll contact region are incorporated. The predicted shell thickness is compared with the literature, which shows good agreement. The thermodynamic calculation to determine equilibrium precipitates over a temperature range has been performed using Thermo-Calc simulation software. The predicted non-isothermal profile from the 1-D transient heat conduction model is used to estimate the precipitation under non-equilibrium conditions using precipitation module (TC-PRISMA) simulation software. The mean particle radius and matrix composition of the precipitates are estimated.

Table of Contents

I

List of Figures

List of Tables

CHAPTER: 1 Introduction

1.1 Background and Motivation

During the production of continuously cast products, special attention should be given to the production of high quality products in terms of both surface and internal quality aspects. The continuous cast strands with crack defect require off-line surface conditioning before the strands are subjected to further processing. Some serious crack defects might not be removed by conditioning; strand with such defects should be either downgraded or scrapped. In addition, further conditioning process affects not only productivity but also yield and increases process cost. Therefore, in order to increase the production rate and quality of the strand, it is necessary to eliminate such crack defects.

It had been recognized that the combination of induced tensile stress and metallurgical embrittlement would be the major reasons for the crack formation which affects the ductility of the strand (Hot ductility) at higher temperature. The hot ductility of the steel is reviewed[1] and three zones of reduced hot ductility are identified. The first of these appears at higher temperature within 50^0C of solidus temperature leading to hot tear. The second range of reduced ductility is in the range from 1200^0C to 600^0C as shown in Fig 1. The second ductility region is sub-divided further into two overlapping temperature zones. One of these affects steel when it is entirely in austenite phase region. The steel which has an alloying element such as titanium, niobium, boron and aluminium influences the formation of nitride, carbide and carbo-nitride precipitates at austenite grain boundary which plays an important role in ductility loss in this region. The emphasis is given to austenite phase region where the strand undergoes bending and straightening process during continuous casting. The third zone occurs in the two-phase austenite to ferrite region below Ar3 temperature.

The thermal history is a major variable affecting hot ductility and time is one of the basic parameters controlling the embrittlement process. The three-zones specified above depends not only on the thermal history and steel composition but also on the size, distribution, location and formation temperature of the precipitates. The thermal stress caused by the non-linear temperature gradients which affect the formation temperature of precipitates. Tensile stresses are induced due to cyclic rapid cooling on the surface whereas due to reheating at the sub surface level.
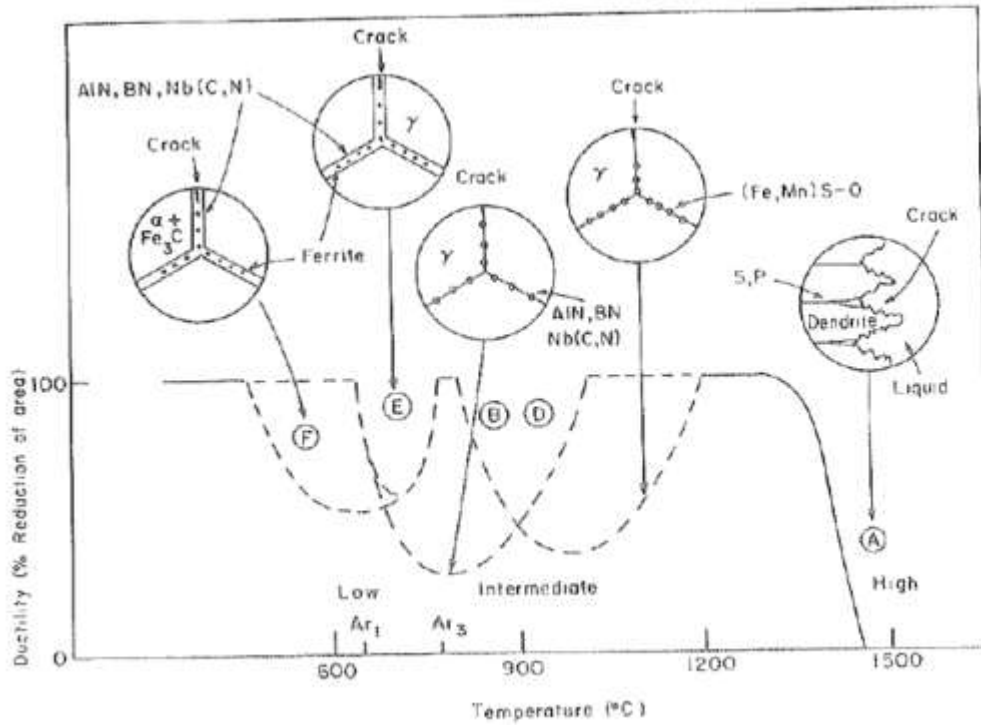
Figure 1.1 Schematic of temperature zone of reduced hot ductility of steel [1]

If the residual tensile stress exceeds the fracture stress, it results in the formation of crack. Hence understanding the fundamentals of crack formation requires analysing the composition, solubility product of different precipitate, precipitate formation in the non-equilibrium and thermal history of steel during the continuous casting process.

Therefore in the present work, the precipitate formation at equilibrium and non-equilibrium conditions for EN-10268 micro-alloyed steel containing niobium, titanium, vanadium is studied along with the strand temperature profile during the continuous casting process.

In the first stage of the work, 1-D transient heat conduction model by enthalpy method is developed for one of the slab casters in JSW Steel Ltd Bellary. The boundary conditions for mould spray and roll regions are described in detail. The model predicts phase fraction, shell thickness and thermal history of the strand. The fundamentals of heat transfer in mould and spray regions are discussed in the section (2.2).

Thermodynamics calculations are performed in the second stage of this work. Thermo-calc simulation software is used for the above grade to predict the stable precipitate phases such as carbides nitrides and carbo-nitrides, formation temperature of precipitate and amount of each phase at equilibrium. The information about solubility product of different precipitates is discussed in the section (2.4).

2

In the final stage of the work, Thermo-calc precipitation model (TC-PRISMA) has been performed for one of the high temperature precipitates to study on the non-equilibrium precipitate formation. The non-isothermal profile obtained from 1-D transient heat conduction model is used as input to precipitate model simulation. TC-PRISMA simulation software provides size, formation temperature of precipitates and matrix composition change during the continuous casting process.

CHAPTER: 2 Literature Review

2.1 Process description

The continuous casting is a process where molten steel is solidified into semi-finished product. The schematic layout of slab casting machine is shown in Fig 2.1. The advantages of continuous casting over ingot casting are superior product quality, higher yield with lower processing cost.
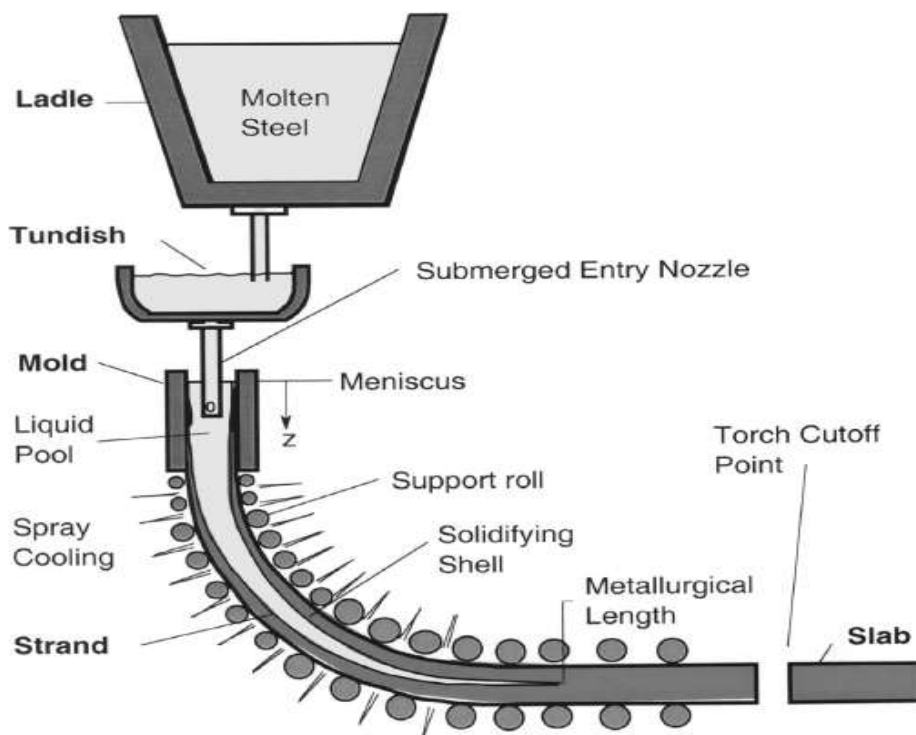
Figure 2.1. Schematic representation of continuous casting machine[2]

The molten steel is poured from a ladle into tundish by way of sliding gate valve mechanism and the stream is protected by a refractory pipe called shroud to avoid re-oxidation. The tundish acts as a reservoir during ladle change and provides seamless continuation of casting. The molten steel is further poured into water cooled copper mould by submerged entry nozzle (SEN). The flow is either controlled by sliding gate mechanism or by stopper rod device. The water cooled copper mould immediately solidifies the liquid steel and forms solid shell. The mould oscillation and lubrication is required to avoid sticking of the solidified shell with the copper mould. As soon as the solidified shell is sufficiently thick to

contain liquid steel, the strand leaves the mould and it is further cooled by water sprays. However, the hot solidified shell has to withstand the pressure arising from the liquid steel within the solidified shell to avoid bulging of strand. Therefore it is necessary to support solidified steel shell by a supporting arrangement which is a set of rollers. In a slab caster, the set of rollers are called segments and the casting machine usually consists of 14 to 15 segments.

2.2. Heat withdrawal in Mould region

2.2.1. Heat flow through the copper mould

Mould is a heart of continuous casting machine. The phenomena of heat transfer in the mould and spray region are required to understand the solidification and shell growth. The mould must extract heat from the steel in a uniform manner with some degree of control. The surface quality of the steel depends on the mould parameters. The active contact length of the mould ranges from 600 to 900mm. To avoid friction between steel shell and the mould, mould flux is added. As the liquid metal solidifies in the water cooled copper mould, there is a loss of contact between steel shell and mould due to liquid contraction which affects the heat transfer. The direction of heat flow from liquid metal is through the following regions

(i) Conduction through the shell,

(ii) Conduction and radiation through the lubrication film

(iii) Conduction through the copper mould

(iv) Convection through cooling water.

Conduction through mould and convection by cooling water greatly affects the mould temperature. Fig 2.2 shows the temperature distribution between molten steel to cooling water.

The heat flux q_{mold} is given by

$$q_{mold} = h_{mould}(T_{hf} - T_{bw}) \tag{2.1}$$

Where, T_{hf} is hot face temperature of mould, T_{bw} is temperature of bulk water and h_{mould} is effective heat transfer coefficient between the hot face of mould wall and cooling water and is given by Eqn (2.2).

$$h_{mould} = \frac{1}{\left(\frac{1}{h_{water}} + \frac{d_{mold}}{k_{mold}}\right)} \qquad (2.2)$$
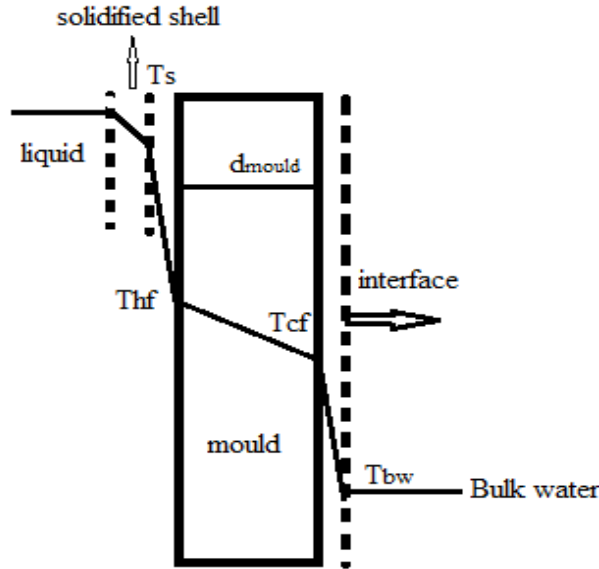
Figure 2.2. Temperature distribution between steel and cooling water

Where, h_{water} is heat transfer coefficient of water, d_{mould} is thickness of mould and k_{mould} is conductivity of mould.

If the temperature of the cooling water at the interface reaches the boiling point, vapour bubbles form which affect the heat transfer. Therefore, the flow parameters of cooling water are controlled to prevent the above said phenomena.

2.2.2. Heat flow through mould flux

The mould flux is a mixture of several oxides, which majorly has silica (SiO_2), lime (CaO) and small amount of Na_2O, CaF_2, and carbon. When it is heated to elevated temperature, the mould flux forms multiple layers such as sintered layer, mushy zone and liquid flux above molten steel. Due to the oscillation of mould, the liquid flux is dragged between mould wall and steel shell. In this position, the mould flux turns into solid near mould wall and remains liquid near steel shell. The amount of solid phase of mould flux increases along the mould length due to the variation in the temperature of mould and steel shell along the length of the mould. Due to steel shell shrinkage and complete formation of solid flux, an air gap is formed at bottom of the mould. A contact resistance is present

6

between mould and solid flux. Figure 2.3 shows the schematic representation of the solid and liquid flux between mould and steel shell.
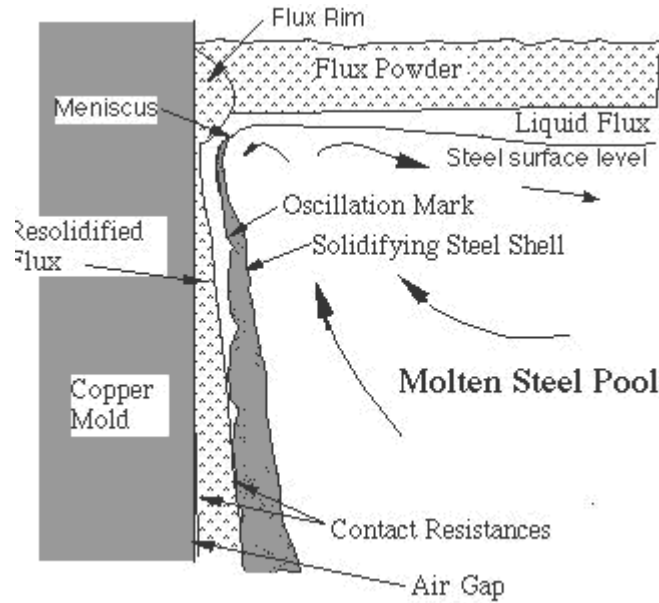
Figure 2.3. Schematic representation of the solid and liquid layer flux between mould and steel shell[3]

The heat flux through the flux layer is given by

$$q_{flux} = h_{gap}(T_s - T_{hf}) \tag{2.3}$$

Where T_s is temperature of the steel shell, T_{hf} is temperature of mould hot face and h_{gap} is effective heat transfer coefficient between mould hot face and steel shell, which is given by solid, liquid layer of mould flux, air gap and contact resistance.

2.3. Heat withdrawal in secondary cooling zone

The following are the ways of extracting heat from the semi solidified strand in the secondary cooling zone which are discussed below

(i) Convection by impingement of water sprays by the pure or air-water mixture

(ii) Conduction through the rolls.

2.3.1. Spray cooling with water

The water sprays are operated in continuous casting on the principle of pressure atomization. The water is forced under pressure through orifice or nozzle that breaks it up into droplets. In slab casters, V-type flat nozzles are used which are normally attached to the header or raiser between support rolls. The spray nozzles are normally divided into different zones to control water flow rate independently.

In slab caster, single and multi-nozzle spray systems are used. The arrangements of single and multi-nozzle systems are shown in Fig 2.4. In single nozzle system, the nozzle provides a wide-angle spray (up to 120°) between successive rolls. This system uses few nozzles, a simple water supply system which is easy to maintain. The multi-nozzle system involves the grouping of many nozzles with a small spray angle at each spray zone. The purpose of multi nozzle system is to provide high water flux with higher casting speed for crack sensitive grades.
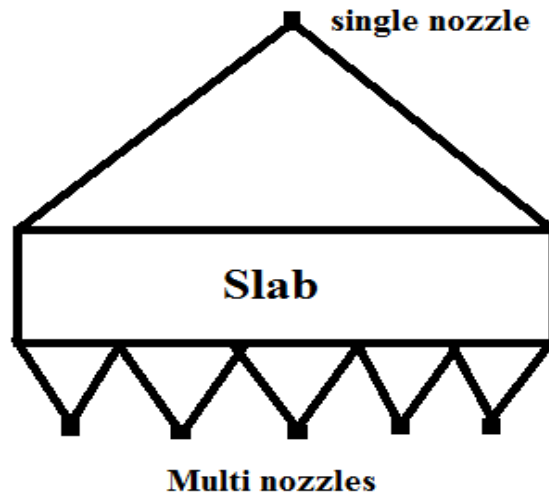
Figure 2.4. Different types of nozzle arrangement

The rate at which heat is extracted from the strand surface by water spray had been measured by many researchers[4]. Experiments have been conducted in spray cooled hot steel plate at steady state and transient conditions. The heat flux due to spray cooling in terms of heat transfer coefficient h_{spray} is given by Eqn 2.1.2.1

$$q_{spray} = h_{spray}(T_s - T_w) \tag{2.4}$$

8

Where T_s is the surface temperature of the strand and T_w is the temperature of spray water. However, the heat transfer coefficient is affected by variables such as water flow rate, nozzle type, nozzle-to-strand distance, water pressure and spray angle whereas the variation of it with the water flux is as shown in Fig (2.5)
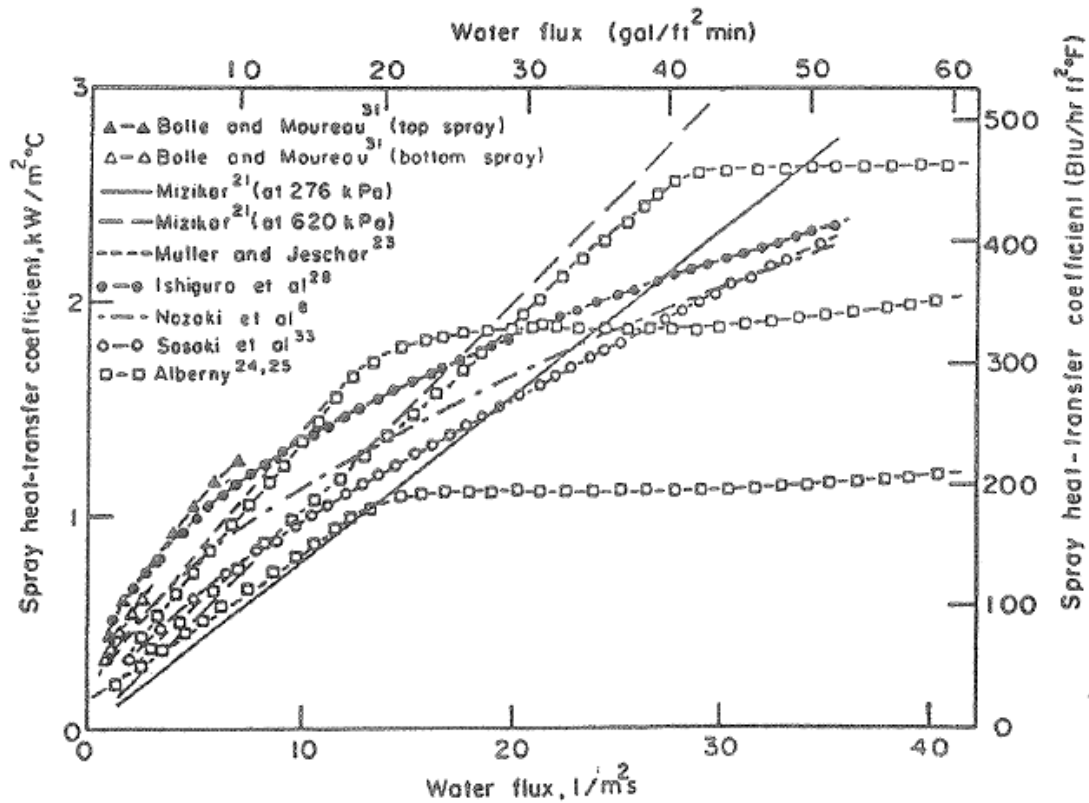
Figure 2.5.Influence of water flux on spray heat transfer coefficient[4]

2.3.2 Spray cooling with water and air (air-mist)

In air-water (air- mist) spray cooling systems, the water is mixed with compressed air in a mixing chamber and passed through the nozzle. A finely atomised (droplet size less than 100 μm) mixture emerges from the nozzle with high pressure and also with wide angle of spread. The volumetric air/water (Q_{air}/Q_{water}) ratio can be varied over a wide range, but typical values used are between 20 to 500 (0.02 to 0.5 Nm^3 air per litre of water). The advantage of air-water sprays as follows

(i) Droplet diameter is more uniform

(ii) Nozzle opening is large which reduces the problem of clogging

(iii) A wide range of flow is possible through a given nozzle size

(iv) Wider areas, such as between support rolls in a slab caster can be cooled uniformly

(v) Less water (about half as much) is required for a given rate of heat extraction compared to conventional sprays.

Heat extraction by air-water mist cooling occurs via convection and radiation through water and air. In Figure 2.6 heat transfer coefficient against water flux ($\dot{w}$) has been plotted with different Q_{air}/Q_{water} ratios where pure water spray is represented by a linear line. It can be clearly seen that at lower water flux, the heat transfer coefficients for air-water cooling is above water spray line since air plays a significant role in the heat transfer.
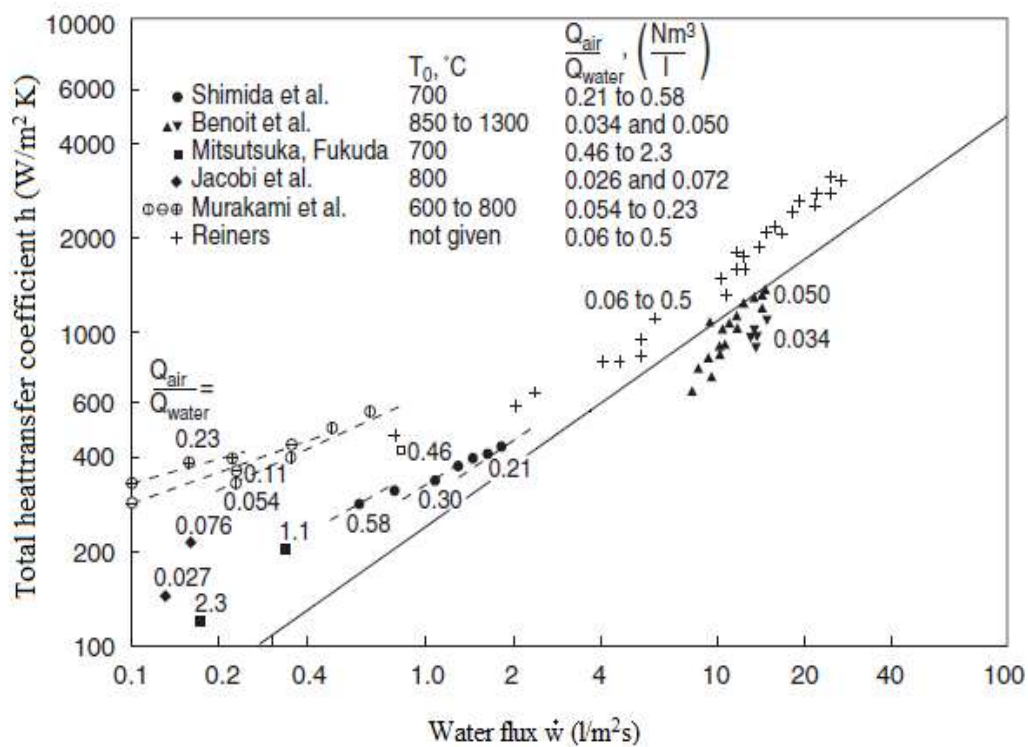
Figure 2.6. Comparison of heat transfer coefficient with varying water flux ($\dot{w}$) and Q_{air}/Q_{water} ratios[5]

At higher water flux and low Q_{air}/Q_{water} ratios, the heat transfer coefficient lies below the spray water line because the effect of air will be small or negligible on heat transfer. Therefore, high heat transfer coefficient for effective strand cooling can be achieved at an optimised combination of water and air.

10

2.3.3. Strand cooling by roll contact

A considerable amount of heat is extracted in slab casting by contact of the strand with rolls. All rolls are water cooled internally except for the rolls of small size located in the upper part of the casting machine where it is spray cooled with water at a higher flow rate. Depending on the number of rolls in a casting machine and type of secondary cooling, 40 to 60% of total heat is removed by the rolls. The spray water flow rate between roll and sleeve thickness of internally water-cooled roller influences heat removal by rolls. As spray water flow rate and sleeve thickness decrease the amount of heat removed by the rolls increases. Other than this, roll pitch, casting speed, bending and alignment status of rolls also affects heat transfer through rolls. Hence the main requirements of support rolls are followed

(i) The diameter and pitches should be such that the inter-roll bulging of the strand should be minimised

(ii) Geometrically the rolls should remain stable; if the rolls are too small in diameter and with length constraints, the rolls may bend due to ferro-static pressure and asymmetrical temperature distribution during rotation.

2.4. Solubility of micro alloy carbides and nitrides

The strengthening effect of micro alloying additions may be produced by dispersion strengthening of fine precipitated particles, or by grain refining, i.e. inhibition of grain growth by second phase particles. Although at a higher temperature, low ductility is observed with fine grain size which reflects the effect of carbides, nitrides and carbo-nitrides precipitate both in grain refining and weakening of the grain boundaries. On the other hand, the action of precipitates may prevent recrystallisation which may result in the formation of coarser grain. In this case, lower ductility would appear associated with the coarser grain size due to grain boundary cavity nucleation by precipitates resulting reduced grain boundary mobility. Therefore, grain size itself is not always controlling the hot ductility that is also influenced by the action of precipitates at grain boundary. In order to understand these effects, it's is necessary to understand the dissolution of various micro alloy carbides nitrides and carbo-nitride precipitates together with knowledge of their precipitation behaviour.

2.2 Solubility of individual compounds

The component parts of micro alloy constituent phase may be present either in solution, in a simple single constituent, or one or more simple or complex constituents. For example, aluminium will react with nitrogen (aluminium and nitrogen are components) to form aluminium nitride (constituent phase). Aluminium nitride shows little or no solubility for micro alloying elements such as niobium and titanium, and only be influenced by the available aluminium and nitrogen. If more stable nitride former is added, this may limit the nitrogen available to the aluminium and may restrict aluminium nitride formation. Under these conditions, there may be two separate nitride phases known as an individual compound. When considering other nitride forming micro alloying elements, such as titanium, vanadium and niobium, considerable mutual solubility exists, and complex carbo-nitrides of these elements is described with help of single constituent phase. However, all of these cases, the thermodynamic stability of the individual components are used to know about complex compounds. Therefore, consideration of their individual solubility's is necessary.

2.2.1 The Solubility product

Consider a constituent MX is an equilibrium with micro alloying element M and interstitial element X in a matrix phase at temperature T.

$$[M]+[X] \longleftrightarrow <MX> \tag{2.5}$$

Where [M] and [X] represents the concentration of M and X dissolved in the austenite matrix, and <MX> represents the constituent. So the equilibrium constant may be written as

$$k = \frac{a_{[M]} \cdot a_{[X]}}{a_{<MX>}} \tag{2.6}$$

Where $a_{[M]}$ and $a_{[X]}$ are the activity of dissolved respective elements, $a_{<MX>}$ is the activity of constituent phase.

The activities in the equation can be expressed in terms of concentration and activity coefficient.

$$a_{[M]} = \gamma_{[M]} \cdot [M] \tag{2.7}$$

$$a_{[X]} = \gamma_{[X]} \cdot [X] \tag{2.8}$$

$$k_s = \frac{\gamma_{[M]} \cdot [M] \cdot \gamma_{[X]} \cdot [X]}{a_{<MX>}} \tag{2.9}$$

It is assumed that the activity coefficient of an element and the pure compound is unity. So equation (2.9) can be written as

$$k_s = [M] \cdot [X] \tag{2.10}$$

Where [M] and [X] is in weight percentage and product of these two is called solubility product k_s. From the experiments such as precipitate extraction, thermodynamic calculation, gaseous equilibrium and solvent extraction, the dissolved amount of alloying element [M] and interstitial element [X] is calculated and the product of [M] and [X] is plotted with different experiment temperatures as shown in Fig (2.7) which shows a linear relationship. From this, the solubility product is expressed in the form of
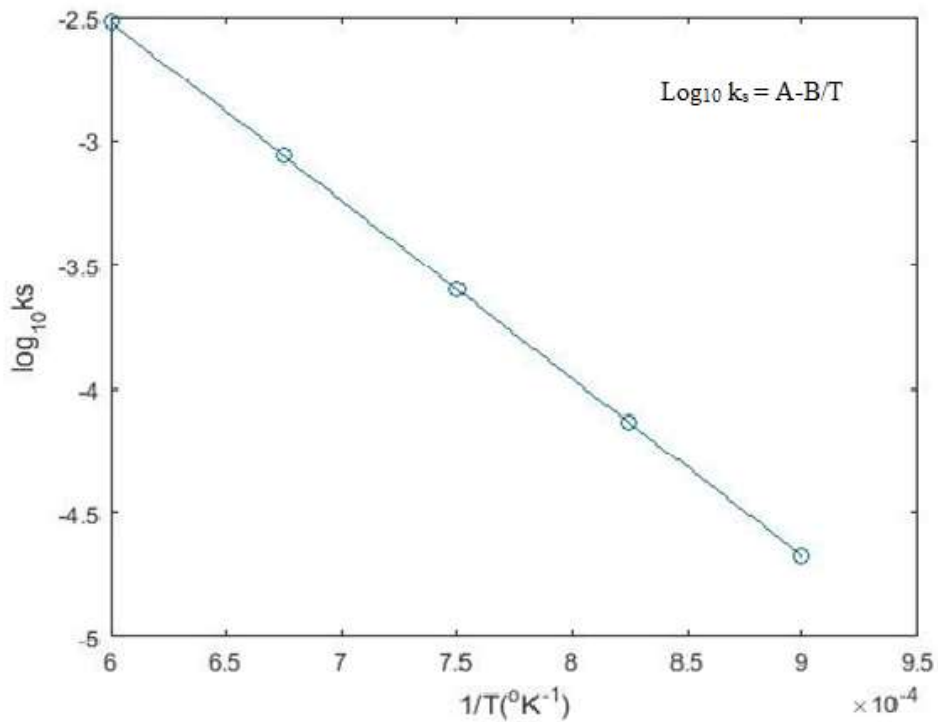
Figure 2.7. Temperature dependence of the solubility product

$$log_{10}k_s = A - \frac{B}{T} \tag{2.11}$$

13

Where A and B are constants in a given system and T is temperature in K. consider Fe-M-X system, for a given temperature and constant A and B in matrix phase, it is possible to construct the boundary between the matrix phase and matrix +<MX> two phase region as shown in Fig (2.8). For each temperature, the solubility product is equal to the product of [M] and [X]. Any alloy composition lying below the curve will be single phase and above to this curve will exist as two-phase region.

In order to calculate the amount of second phase particle (MX) and solute concentration, serious of mass balance equations have to be performed. For example, consider Fe-Ti-N system, where titanium and nitrogen react in terms of atomic mass percentage, which forms titanium nitride (TiN) precipitate, then the mass balance relationships are

$$[Ti] + Ti_{TiN} = Ti_T \tag{2.12}$$

$$[N] + N_{TiN} = N_T \tag{2.13}$$
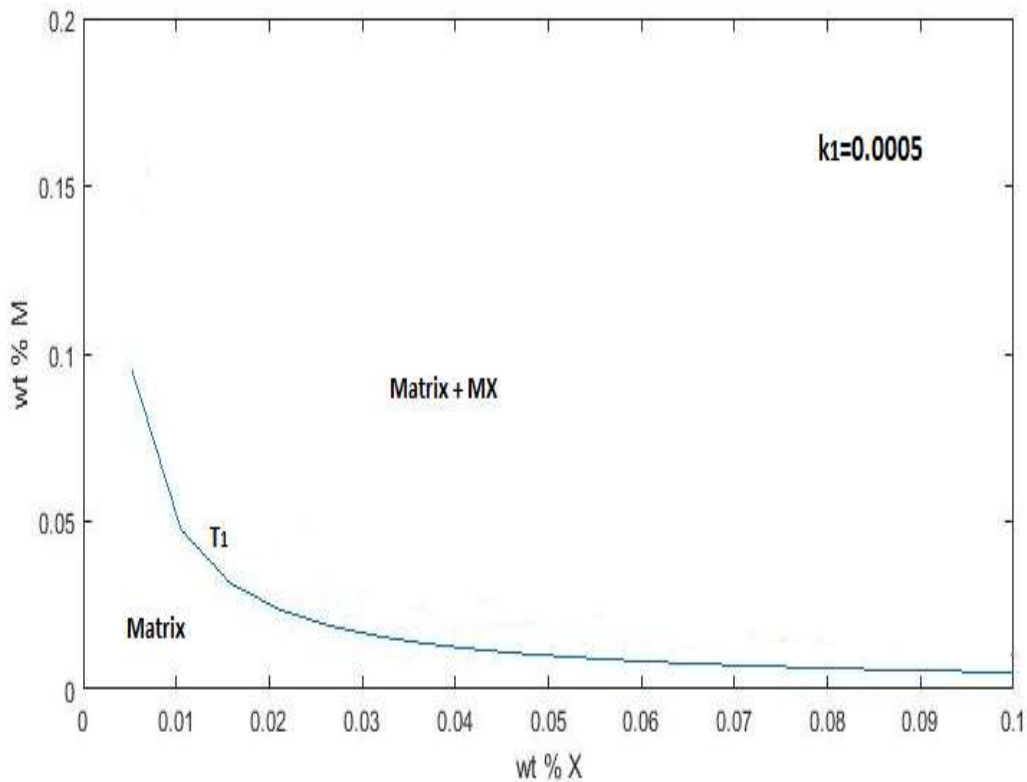
Figure 2.8. Solubility diagram showing the single phase and two phase field for Fe-M-X system

$$Ti_{TiN} \frac{A_N}{A_{Ti}} = N_{TiN} \tag{2.14}$$

14

$$< TiN > = Ti_{TiN} \frac{(A_{Ti} + A_N)}{A_{Ti}} \quad \text{(2.15)}$$

$$< TiN > = N_{TiN} \frac{(A_{Ti} + A_N)}{A_N} \quad \text{(2.16)}$$

From equation (2.12-2.16)

$$k_s = [Ti][N]$$

$$= (Ti_T - Ti_{TiN})(N_T - N_{TiN})$$

$$= (Ti_T - Ti_{TiN})(N_T - \frac{A_N}{A_{Ti}} Ti_{TiN}) \quad \text{(2.17)}$$

Where

Ti_T= wt% Ti in the alloy

$[Ti]$= wt% Ti dissolved in the matrix

Ti_{TiN}= wt% Ti present as TiN

N_T= wt% N in the alloy

$[N]$= wt% N dissolved in the matrix

N_{TiN} = wt% N present as TiN

A_{Ti}= atomic mass of titanium

A_N= atomic mass of nitrogen

<TiN> = wt% of TiN as a precipitate

The total amount of Titanium and nitrogen in the steel is known. From equation (2.16) the wt% of TiN precipitate can be calculated.

2.2.2. Solubility data for different carbide and nitrides

(a) Aluminium nitride

Aluminium is primarily added as a deoxidizer but it also forms aluminium nitride precipitate. The solubility data for aluminium nitride in austenite has been evaluated by many workers[6] using either classical thermodynamics methods involving equilibration with gaseous atmospheres of known nitrogen activity or chemical methods designed to evaluate nitrogen in the form of nitride, such as the Beeghley ester-halogen technique. This involves the dissolution of the steel matrix, usually in a bromine-methanol solution, filtration of the residue, and distillation of the residue in an alkaline solution, where the nitrogen is converted

into ammonia which is determined volumetrically. The solubility data of aluminium nitride in austenite is given in table (2.1).

Table 2.1. Solubility relationships for aluminium nitride in austenite[6]

Logarithm of solubility product ($log_{10}k_s$)	Method	Temperature range (^{o}C)
-7400/T + 1.95	Sieverts	1050-1350
- 7184/T + 1.79	Beeghley	800-1300
- 6770/T + 1.03	Beeghley	810-1260
-7750/T + 1.80	Beeghley	900-1350
- 6180/T + 0.73	Beeghley	900-1200
- 7500/T + 1.48	Beeghley	950-1300
- 9200/T + 2.92	Beeghley	850-1300

(b) Titanium Nitride and Carbide

Titanium is used for grain refinement and precipitation hardening by the formation of titanium carbide and titanium nitride. This plays important role since titanium nitride precipitate first and consumes all nitrogen so that no other nitride forms during cooling. On comparing solubility of titanium nitride with other micro alloying element, the titanium nitride is more stable at high temperature. The expressions for the solubility product of titanium nitride have been obtained in liquid, austenite and ferrite phase which are given in table (2.3). One of the difficulties associated with these data is related to the presence of nitrogen in the steel, this has to be considered when interpreting experimental data.

Table 2.2. solubility product for titanium nitride and carbide[6]

Titanium nitride	
Logarithm of solubility product	Method
Liquid	
-16586/T + 5.90	Gaseous equilibrium
Austenite	
-15020/T + 3.82	Gaseous equilibrium
- 8000/T + 0.32	Precipitate extraction
Titanium carbide	
Austenite	
-7000/T + 1.71	Precipitate extraction
-10475/T + 5.33	Gaseous equilibrium
-10300/T + 5.12	Precipitate extraction
Ferrite	
-9575/T + 4.40	Thermodynamic calculation

(b) Niobium nitride and carbide

Addition of niobium in steel provides solid solution strengthening and precipitation hardening. Another important function of niobium is detaining of recrystallization. Niobium may precipitate as carbide, nitride and carbo-nitride. The solubility data for niobium nitride and carbide are given in table (2.3). Different methods have been used to obtain solubility data in austenite and ferrite phase. From these data's, it can be seen that niobium nitride as well as niobium carbide will be less soluble in ferrite than in austenite with respect to temperature.

Table 2.3. Solubility product for niobium nitride and carbide[6]

Niobium nitride	
Logarithm of solubility product	Method
Austenite	
-8500/T + 2.80	Gaseous equilibrium
- 10230/T + 4.04	Gaseous equilibrium
-7000/T + 1.71	Solvent extraction
Ferrite	
-12230/T + 4.96	Thermodynamic calculation
Niobium carbide	
Austenite	
-6770/T + 2.26	Precipitate extraction
-7900/T + 3.42	Gaseous equilibrium
-7510/T + 2.96	Thermodynamic calculation
Ferrite	
-10960/T + 5.43	Thermodynamic calculation
-9930/T + 3.90	Thermodynamic calculation

(c) Vanadium nitride and carbide

Vanadium is added to provide solid solution strengthening and dispersion hardening in steel. This affects the austenite recrystallization by precipitating austenite and ferrite interface. The solubility product of vanadium nitride and carbide in austenite matrix is given in table (2.4). However, for micro alloyed steel with significant manganese content, equation (2.18) is recommended, because the solubility product increased slightly with increasing manganese content in steel. It is observed that reducing manganese content to zero would reduce the solubility product and no variation is observed by changing the carbon content with temperature.

$$log_{10}k_s = -\frac{8330}{T} + 3.40 + 0.12[Mn\%] \tag{2.18}$$

A significant feature is that the solubility of vanadium carbide in austenite is considerably higher than other micro alloy carbides and nitrides resulting in vanadium carbide being completely dissolved even at low austenite temperature

Table 2.4. solubility product for titanium nitride and carbide[6]

Vanadium nitride	
Logarithm of solubility product	Method
-8330/T + 3.46	Precipitate extraction
-7070/T + 2.27	Thermodynamic calculation
- 7840/T + 3.02	Precipitate extraction
-8700/T + 3.63	Gaseous equilibrium
Vanadium carbide	
Austenite	
-9500/T + 6.72	Gaseous equilibrium
-10800/T + 7.06 (V$_4$C$_3$)	Gaseous equilibrium
-9407/T + 5.65 (V$_4$C$_3$)	Precipitate extraction
Ferrite	
-12265/T + 8.05	Thermodynamic calculation

2.2.3 Comparison of solubility of micro alloy carbides and nitrides

The solubility product of the micro alloy carbides and nitrides are compared in Fig (2.9). The individual solubility of the micro alloy carbides and nitrides shows clear understanding of the selection of alloying elements for specific application. Hence there are several important points that can be observed from the assembled data.

(i) Comparison of solubility data shows that the nitride is more stable than the carbide in austenite. The solubility product difference between micro alloy carbide and nitrides differ significantly depending upon the alloy elements. A large difference is observed between vanadium carbide and vanadium nitride and between titanium carbide and titanium nitride. The difference between solubility's of niobium carbide and niobium

19

nitride is much less.

(ii) The aluminium carbide has never been reported in this comparison, indicating that aluminium carbide is more soluble than other carbides in steel.

(iii) Titanium nitride is more stable than other micro alloy carbides and nitrides and it is observed that the titanium nitride even can form in the liquid phase.

(iv) Vanadium carbide is more soluble than other micro alloy carbides and nitrides in austenite and ferrite phase.
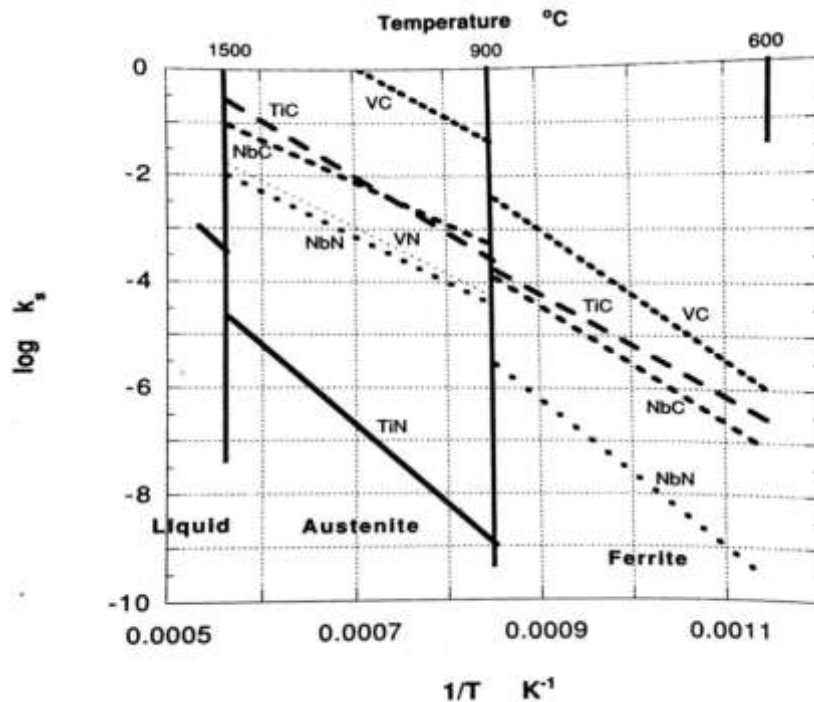
Figure 2.9. Comparison of the solubility products of the micro alloy carbides and nitrides[6]

2.3 Mutually exclusive compounds

Most of the micro alloy carbides and nitrides have a face centred cubic structure that shows mutual solubility with each other. However, aluminium nitride has a hexagonal structure. In steel containing aluminium and other micro alloying addictive's, there are two different type of precipitates are observed, i.e. hexagonal aluminium nitride and face centred cubic carbides and nitrides. These are mutually exclusive compounds.

For example, consider Fe-Al-V-N system, the solubility product for aluminium nitride and vanadium nitride are defined as

$$[V] + [N] \longleftrightarrow <VN> \qquad FCC$$

$$k_V = [V][N] \qquad\qquad (2.19)$$

20

$$[Al] + [N] \longleftrightarrow < AlN > \quad \text{Hexagonal}$$
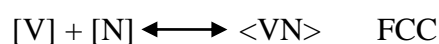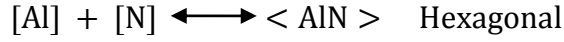
$$k_{Al} = [Al][N] \tag{2.20}$$

Aluminium nitride will be formed when the product of dissolved aluminium and nitrogen exceeds k_{Al} and vanadium nitride will be formed when the product of dissolved vanadium and nitrogen exceeds k_V at given temperature. From the solubility data, it is clear that the solubility product of aluminium nitride is lower than vanadium nitride so aluminium nitride forms first followed by vanadium nitride. It should be noted that the activities of both nitrides remain unity because they are separate nitrides with no mutual solubility. With help of solubility product and mass balance equations, the dissolved aluminium vanadium and nitrogen can be calculated.

The total nitrogen content N_T in the steel is the sum of the dissolved nitrogen $[N]$, the nitrogen present as aluminium nitride N_{AlN} and vanadium nitride N_{VN}. i.e

$$N_T = [N] + N_{AlN} + N_{VN} \tag{2.21}$$

The weight percent nitrogen as aluminium nitride can be written as weight percentage of aluminium as aluminium nitride multiplied by their relative atomic masses so,

$$N_{AlN} = \frac{14}{27} Al_{AlN} \tag{2.21}$$

Similarly,

$$N_{VN} = \frac{14}{51} V_{VN} \tag{2.22}$$

Substituting these values into equation (2.19) gives,

$$N_T = [N] + \frac{14}{27} Al_{AlN} + \frac{14}{51} V_{VN} \tag{2.23}$$

The aluminium present as aluminium nitride will be the difference between total aluminium content Al_T and dissolved aluminium content $[Al]$. Similar kind of relationship can be written for vanadium,

$$N_T = [N] + \frac{14}{27} (Al_T - [Al]) + \frac{14}{51} (V_T - [V]) \tag{2.24}$$

From the individual solubility product as indicated in equation (2.18-2.19), then the equation (2.24) can be written as,

$$N_T = [N] + \frac{14}{27}\left(Al_T - \frac{k_{Al}}{[N]}\right) + \frac{14}{51}\left(V_T - \frac{k_V}{[N]}\right) \tag{2.25}$$

In equation (2.25) total nitrogen N_T, aluminium Al_T and vanadium V_T are known, the only unknown is dissolved nitrogen $[N]$ content that can be calculated by this expression. Similar expressions can be formed for dissolved aluminium $[Al]$ for a given temperature and composition of steel. It is also possible to calculate the phase boundaries of the γ (austenite), γ + VN, γ + AlN and γ + VN + AlN and the range of composition over which the two nitrides will co-exist. The phase boundaries calculated from the solubility data for two different nitrogen content at 900°C is shown in Fig (2.10).
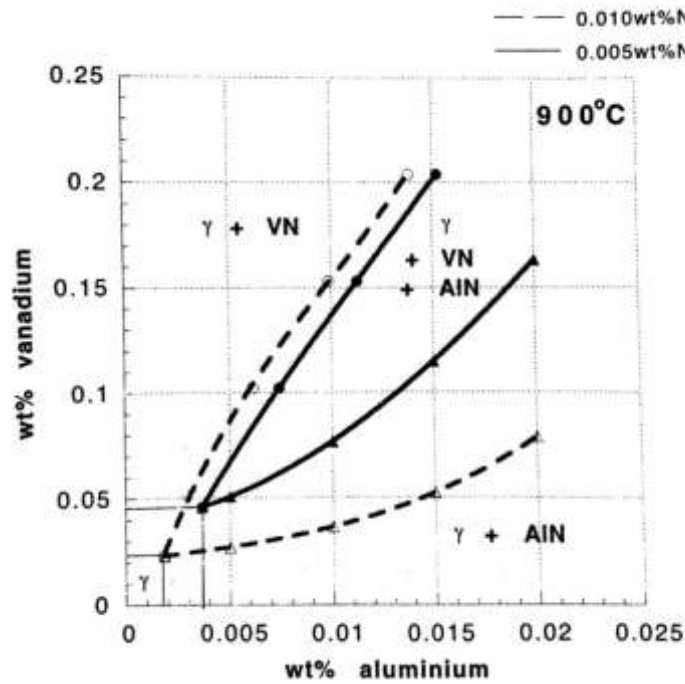
Figure 2.10. Calculated limit of the γ + VN + AlN phase field for two different level of nitrogen at 900°C[6]

The phase boundaries between austenite, two phase and three phase regions are also clearly shown. The effect of vanadium on aluminium and aluminium on vanadium are shown by the boundary between two phase and three phase region. Reducing the nitrogen content of steel expands the austenite range with respect to the aluminium and vanadium content. An increase

in the austenitising temperature also gives a similar effect to that of reducing the nitrogen content

2.4 Carbo-nitrides with extended mutual solubility

The micro alloying elements like Ti, V and Nb, all react with both carbon and nitrogen and form carbides and nitrides and their individual solubility has been described in section (2.2.2). Some of the carbides and nitrides have the same cubic crystal structure and have similar lattice parameter leading to the formation of solid solution (carbo-nitrides) and shows extensive mutual solubility depending on the carbon/nitrogen ratio.

The fraction of carbides and nitrides can be measurable by considering the individual solubility product as defined by following expression in Fe-Nb-C-N system

$$k_1 = \frac{a_{[Nb]}a_{[c]}}{a_{<NbC>}} \tag{2.26}$$

$$k_2 = \frac{a_{[Nb]}a_{[N]}}{a_{<NbN>}} \tag{2.27}$$

Where k_1 and k_2 are the equilibrium constants for the carbide and nitride respectively.

The difference between the mutually exclusive precipitates and extended mutual solubility is that the activity of niobium carbide (*NbC*) and niobium nitride (*NbN*) is not unity. If the solid solution is considered, the activity of carbide and nitride can be represented by their respective fractions in the carbo-nitride. i.e. *x* and (*1-x*). Assuming the activity coefficient of niobium, carbon and nitrogen dissolved in the austenite are unity, the solubility products for *NbC* and *NbN* can be written as

$$k_1 = \frac{a_{[Nb]}a_{[C]}}{x} \tag{2.28}$$

$$k_2 = \frac{a_{[Nb]}a_{[N]}}{(1-x)} \tag{2.29}$$

Using mass balance equations and stoichiometric ratios,

$$Nb_T = [Nb] + Nb_{NbCN} \tag{2.30}$$

$$Nb_{NbC} = x.Nb_{NbCN} \tag{2.31}$$

23

$$Nb_{NbN} = (1 - x).Nb_{NbCN} \tag{2.32}$$

$$C_T = [C] + C_{NbCN} \tag{2.33}$$

$$N_T = [N] + N_{NbCN} \tag{2.34}$$

$$C_{NbC} = \frac{12}{93} Nb_{NbC} \tag{2.35}$$

$$N_{NbN} = \frac{14}{93} Nb_{NbN} \tag{2.36}$$

Where 12, 14 and 93 are the relative atomic masses of carbon, nitrogen and niobium respectively. So equation (2.28) and (2.29) can be written as

$$x.k_1 = [Nb]\left(C_T - x.\frac{12}{93}(Nb_T - [Nb])\right) \tag{2.37}$$

$$(1 - x).k_1 = [Nb]\left(N_T - (1 - x).\frac{14}{93}(Nb_T - [Nb])\right) \tag{2.38}$$

Table 2.5. Effect of steel chemistry and temperature on the carbide fraction of carbo-nitride[6]

Steel composition (wt%)			Temperature	[Nb] (wt%)	NbCN	x
C	N	Nb	(°C)		(wt%)	
0.10	0.005	0.03	950	0.0062	0.0238	0.665
0.10	0.010	0.03	950	0.0046	0.0254	0.496
0.10	0.005	0.08	950	0.0074	0.0726	0.753
0.10	0.010	0.08	950	0.0056	0.0744	0.579
0.80	0.005	0.03	950	0.0011	0.0289	0.960
0.80	0.010	0.03	950	0.0010	0.0290	0.916
0.10	0.010	0.03	1100	0.0225	0.0075	0.483
0.10	0.010	0.08	1100	0.0272	0.0528	0.564
0.80	0.005	0.03	1100	0.0055	0.0245	0.945
0.80	0.010	0.03	1100	0.0052	0.0248	0.893
0.80	0.005	0.03	1200	0.0134	0.0166	0.938
0.80	0.010	0.03	1200	0.0126	0.0174	0.882

The calculated values of dissolved niobium and carbo-nitride are shown in table (2.5) for different steel chemistry and temperature. However, the effect of chemistry and temperature on the dissolution of niobium carbide and carbide fraction of carbo-nitride, the following observations are made.

(i) The fraction of carbide x in carbo-nitride changes with the change in niobium, carbon and nitrogen content and austenitising temperature. The decrease in carbide fraction value x is observed with increasing temperature because at high temperature nitrides are more stable.

(ii) Increasing the austenitising temperature from 950°C to 1100°C, increases the dissolved niobium content and decreases the undissolved niobium content.

(iii) Increasing the nitrogen content of 0.1% C steels from 0.005wt% to 0.01wt% decreases the dissolved nitrogen content.

(iv) Increasing the niobium content of 0.1% C steel from 0.03wt% to 0.08wt% increases the amount of niobium carbo-nitride, and also slight change in the amount of dissolved niobium.

(v) The large increase in the carbon content causes decrease in the dissolved niobium content and increase in the carbide fraction in the range of 0.882 to 0.96.

The amount of niobium as niobium carbide and niobium as niobium nitride when both are present as separate compound, that can be obtained from the dissolved niobium content through the use of solubility product. These data's are compared with the weight percentage of niobium in niobium carbo-nitride and the differences between these two are shown in Fig (2.11).

For mutually exclusive precipitates, the product of *[C]* and *[Nb]* is solubility product k_1, and the product of *[N]* and *[Nb]* is solubility product k_2. For mutually soluble carbo-nitride, the product of *[C]* and *[Nb]* is $x.k_1$ (x is carbide fraction) and product of *[N]* and *[Nb]* is $(1-x).k_1$ (*(1-x)* nitride fraction). Comparison of these two shows, when the carbides and nitrides are mutually soluble, that must be expected from a reduction in the solubility product, i.e. k_1 to $x.k_1$, and k_2 to $(1-x).k_2$. Therefore the formation of carbo-nitride increases the volume fraction of precipitate at a given temperature and also increases the temperature required for total dissolution of the precipitate.
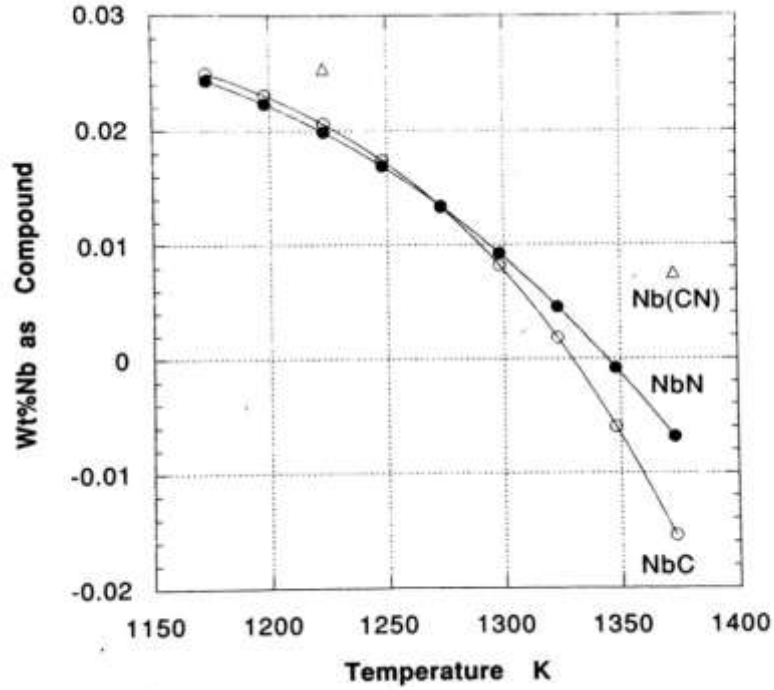
Figure 2.11. Comparison of niobium carbide and niobium nitride with niobium carbo-nitride [6]

2.5 Complex carbo-nitrides

The carbides, nitrides and carbo-nitrides appear to exhibit mutual solubility because of the similarity in crystal structure and lattice parameters. The formation of carbo-nitrides with single micro alloying additions has been discussed previously. In steel containing carbon and nitrogen as an interstitial element and more than one micro alloying elements, a complex carbo-nitrides can be formed which is a solid solution of carbides and nitrides

Consider steel having Titanium (*Ti*), Niobium (*Nb*), carbon (*C*) and nitrogen (*N*). The two micro alloying elements from carbides, nitrides and their respective solubility product expressions are

$$[Ti] + [C] = < TiC > \qquad k_1 = \frac{[Ti][C]}{a_{TiC}} \qquad (2.39)$$

$$[Nb] + [C] = < NbC > \qquad k_2 = \frac{[Nb][C]}{a_{NbC}} \qquad (2.40)$$

$$[Ti] + [N] = < TiN > \qquad k_3 = \frac{[Ti][N]}{a_{TiN}} \qquad (2.41)$$

26

$$[Nb] + [N] = <NbN> \qquad k_4 = \frac{[Nb][N]}{a_{NbN}} \qquad (2.42)$$

Consider the formation of complex carbide of titanium and niobium

$$x[Ti] + (1-x)[Nb] + [C] = Ti_xNb_{(1-x)}C \qquad (2.43)$$

And for complex nitride of titanium and niobium

$$y[Ti] + (1-y)[Nb] + [N] = Ti_yNb_{(1-y)}N \qquad (2.44)$$

Where x and y are the titanium element fractions of carbide and nitride respectively. If the carbide and nitride forms the carbo-nitride then expression will be,

$$xz[Ti] + (1-x)z[Nb] + z[C] + y(1-z)[Ti] + (1-y)(1-z)[Nb] \qquad (2.45)$$
$$+ (1-z)[N] = Ti_{xz+y(1-z)}Nb_{(1-x)z+(1-y)(1-z)}C_zN_{(1-z)}$$

Where, z and $(1\text{-}z)$ are the carbon and nitrogen element fraction in carbo-nitride respectively. Consider the assumption of an ideal solution in the complex carbo-nitrides, the activity of these compounds can be written as

$$a_{TiC} = xz \qquad (2.46)$$

$$a_{NbC} = (1-x)z \qquad (2.47)$$

$$a_{TiN} = y(1-z) \qquad (2.48)$$

$$a_{NbN} = (1-y)(1-z) \qquad (2.49)$$

Substituting equation (2.46-2.49) into equation (2.39-2.42) gives

$$k_1 = \frac{[Ti][C]}{xz} \qquad (2.50)$$

$$k_2 = \frac{[Nb][C]}{(1-x)z} \qquad (2.51)$$

$$k_3 = \frac{[Ti][N]}{y(1-z)} \qquad (2.52)$$

$$k_4 = \frac{[Nb][N]}{(1-y)(1-z)} \qquad (2.53)$$

Using mass balance equations will provide serious of equations and capable of calculating the carbide and nitrides fraction of titanium and niobium micro alloying element similar to the extended mutual solubility of carbo-nitrides.

2.6 Precipitation growth

The amount of undissolved carbide, nitride and carbo-nitride for any given steel composition and temperature can be calculated from the solubility data of respective compound. Although the kinetics of precipitation is influenced by cooling rate i.e, thermal history of strand during the continuous casting process and the rate of precipitation is a function of nucleation sites, diffusivity, solubility product and driving force. At higher temperature, diffusivity is high and nucleation sites are less so precipitates are more likely to grow. But with decreasing temperature, nucleation sites become more but diffusivity comes down. which leads to increase in nucleation rate. Therefore, the high temperature precipitates such as titanium nitride, titanium carbide, niobium nitride, niobium carbide and aluminium nitride nucleates mostly at grain boundary. The low temperature precipitates such as vanadium carbide and vanadium nitride forms at grain interiors and grain boundaries or dislocations if deformation is applied.

The presence of precipitate has direct influence on grain structure at elevated temperature. The size and volume fraction of the precipitate is important in controlling grain size and enhancing the dispersion strengthening which may contribute to achieve higher yield strength.

Another important phenomenon that can affect the particle size are Ostwald ripening. This phenomenon of Ostwald ripening relates to the increase in particle size occurs at a constant volume fraction of precipitate and result in loss of performance of particle

2.7 Introduction to Thermo-calc

Thermo-calc is a software package used to perform thermodynamic calculations for a variety of calculations including equilibrium of stable phases, composition, amount of phases, activity, enthalpies, heat capacity of the elements, liquidus, solidus temperature and driving force for the phase transformation. The aim of the software package is to make efficient thermodynamic calculations for the industrial applications. This is especially designed for the multi component systems with 40 elements and 1000 species with different

stoichiometric phases. This works with the concept of minimizing of free energy so called global minimization technique as shown in Fig (3.1).
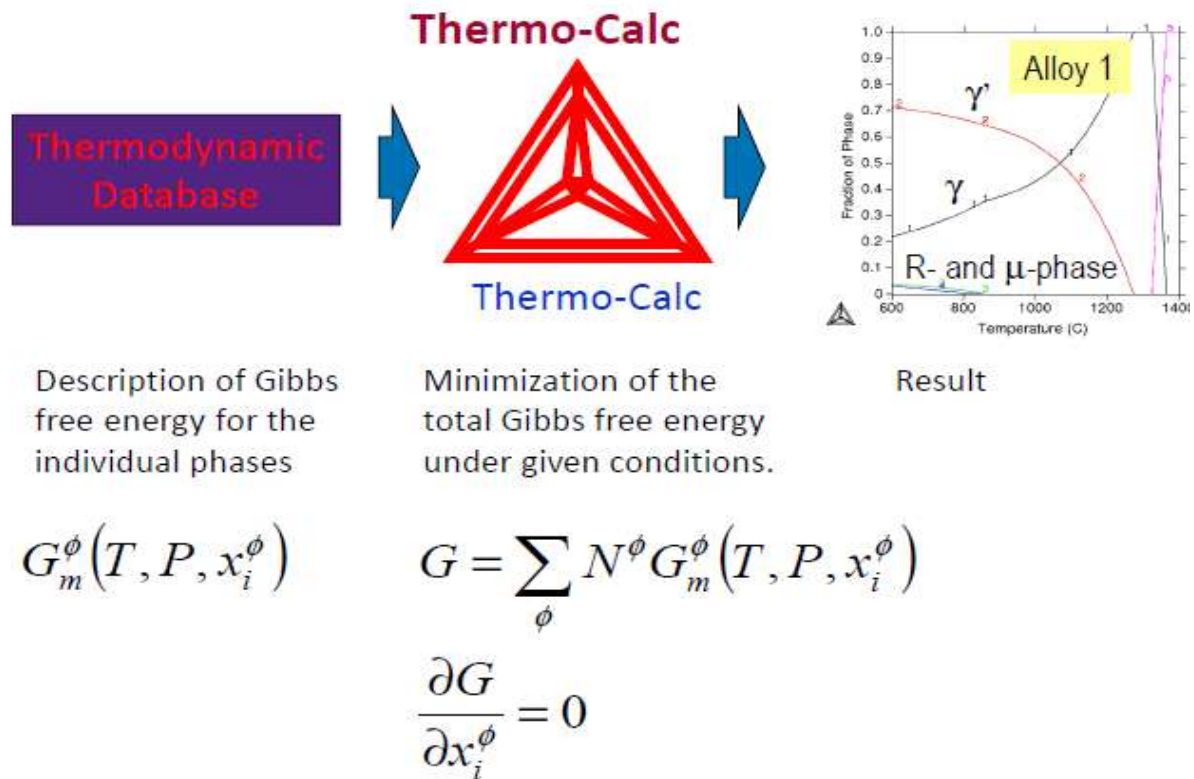

Figure 2.11. The working principle of thermo-calc[7]

Experimental and theoretical data have been used to predict equilibrium of different phases. The experimental data consists of phase equilibrium (phase diagram) for binary and ternary systems (liquidus, solidus and phase boundary), thermodynamic data for compounds, stoichiometric phases and activity measurements. Theoretical data can be performed by estimations and Ab initios calculation. Different database is available out of which steels/Fe-alloys v8.1 (TCFE8) and steel/Fe-alloys mobility v3.0 (MOBFE3) mobility database have been used to assess the steel and their alloy systems.

Thermo-calc software is available in two different modes which are graphical and console mode. In graphical mode steps which are needed to calculate the equilibrium, phase diagram and property diagram will be generated by the system utility itself and only the necessary values for the calculations need to be given. In the case of console mode, all function has to be assessed by giving command to the system utility.

2.8. Thermo-Calc Precipitation Module

Thermo-Calc Precipitation module (TC-PRISMA) is a simulation software used to calculate the precipitation kinetics in the multi-component or multiphase system under isothermal and non-isothermal condition. This module works with help of thermodynamic and a diffusion calculation where the element information is given by Thermo-Calc and mobility data is obtained from Dictra module. TC-PRISMA uses the Langer-Schwartz theory and the Kampmann-Wagner numerical approach. The rate of nucleation J is calculated based on the nucleation theory is given by

$$J = N_o . z . \beta . e^{\frac{G^*}{kT}} . e^{\frac{\tau}{t}} \tag{2.53}$$

Where

N_o = Number of possible nucleation sites

z = Zeldovich factor (based on thermal vibration)

β = atomic attachment rate

G^* = Critical nucleation energy

T = temperature (K)

τ = time constant

t = time (s)

TC-PRISMA is developed by Java language which is simpler to use in graphical user interface. With few steps, the input can be set and simulation is performed. The required inputs and possible outcomes by TC-PRISMA are shown in Table (2.6).

Table 2.6. Inputs and outputs of precipitation model

Input		Output
Alloy composition		Particle size distribution
Temperature		Number density
Simulation time	**TC-PRISMA**	Average particle radius
Thermodynamic data		Volume fraction
Kinetic data		Matrix composition
Property data		Precipitate composition
Nucleation sites		Nucleation rate

CHAPTER: 3 Model formulation

3.1 Heat Transfer

In present work, the model computes 1-D transient heat conduction through solidifying steel shell by enthalpy way. The heat transfer through the wide face is symmetric and only half thickness of the slab has been considered for model formation. A slice of strand is moved with a particular casting speed from meniscus to last roll of the machine where the strand is exposed to different boundary conditions in mould and spray region. This model tracks the enthalpy change due to different boundary conditions and back calculates the temperature change of strand from the corresponding enthalpy.

3.1.1 Assumptions

The following assumptions are made to simplify the mathematical modelling

  (i) The average mould temperature as a function of distance has been assumed from the available 2-D model [3] as shown in Fig (3.1).

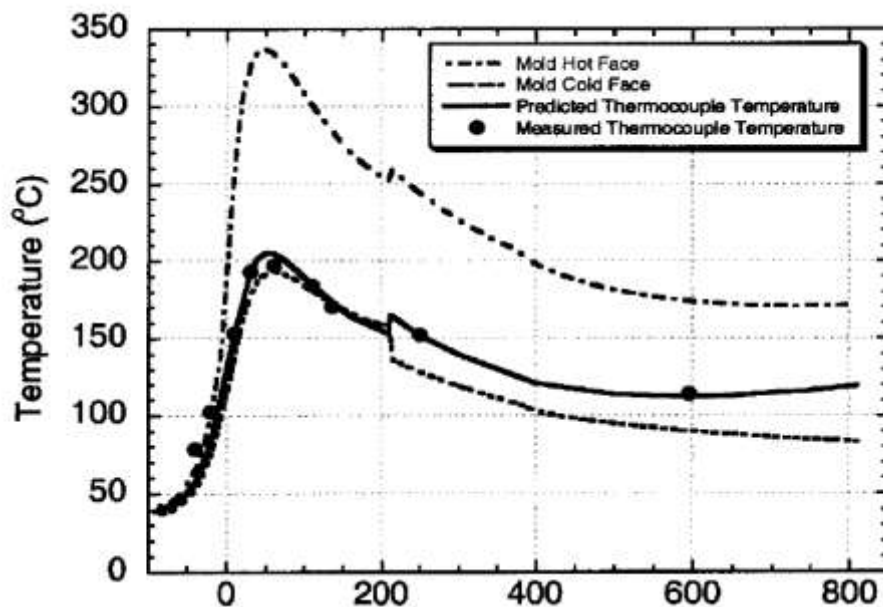 (ii) There is no dendritic formation during solidification and the interface between the liquid and solid is planar.

Figure 3.1. 2-D model result of mould hot and cold face temprature[3]

(i) It has been assumed that the effective thermal conductivity of the liquid is seven times the thermal conductivity of solid $(k_l = 7 * k_s)$ to account the convective heat flow in molten steel.

(ii) Segregation is not considered during solidification and phase fraction is calculated based on the lever rule.

3.1.2 Governing Equation

Heat flow in the solidified steel shell is governed by 1-D transient heat conduction equation, where the effective conductivity of steel is dependent on temperature and phase fraction discussed in section 3.1.4.

$$\rho_{steel} \frac{\partial H}{\partial t} = \frac{\partial}{\partial x}\left(k_{eff} \frac{\partial T}{\partial x}\right) \tag{3.1}$$

The model domain (half thickness of the strand) is shown in Fig (3.2). The applied boundary conditions in governing equations are,
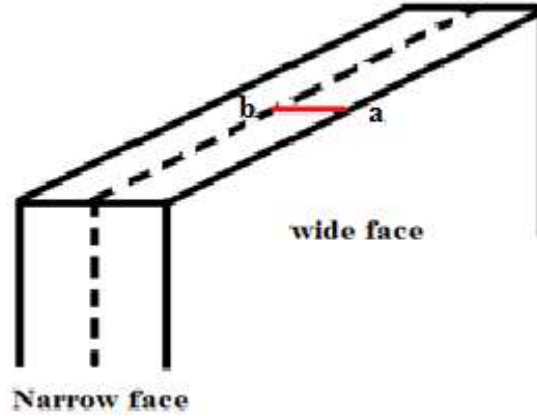

Figure 3.2. Schematic representation of the model domain

$$\left.\frac{\partial T}{\partial x}\right|_b = 0 \tag{3.2}$$

$$h(T_s - T_{inf}) = -q \tag{3.3}$$

Where T_s is solidified steel shell surface temperature and h is heat transfer coefficient. Different h are evaluated as a function of strand position below the meniscus, as discussed in

32

section 3.4. The governing equation is discretized by using finite volume method where half control volume is considered for boundary nodes ($\Delta x/2$).

3.1.3 Enthalpy versus temperature plot

The enthalpy of a micro alloyed steel composition is given in Table 3.1 is plotted against temperature by using Thermo-calc simulation software that has different phase regions. This curve has been fitted with different linear expressions for a single and multiple phase transformation regions with temperature and enthalpy is taken as a function of each other (T=T (H) and H=H (T)).
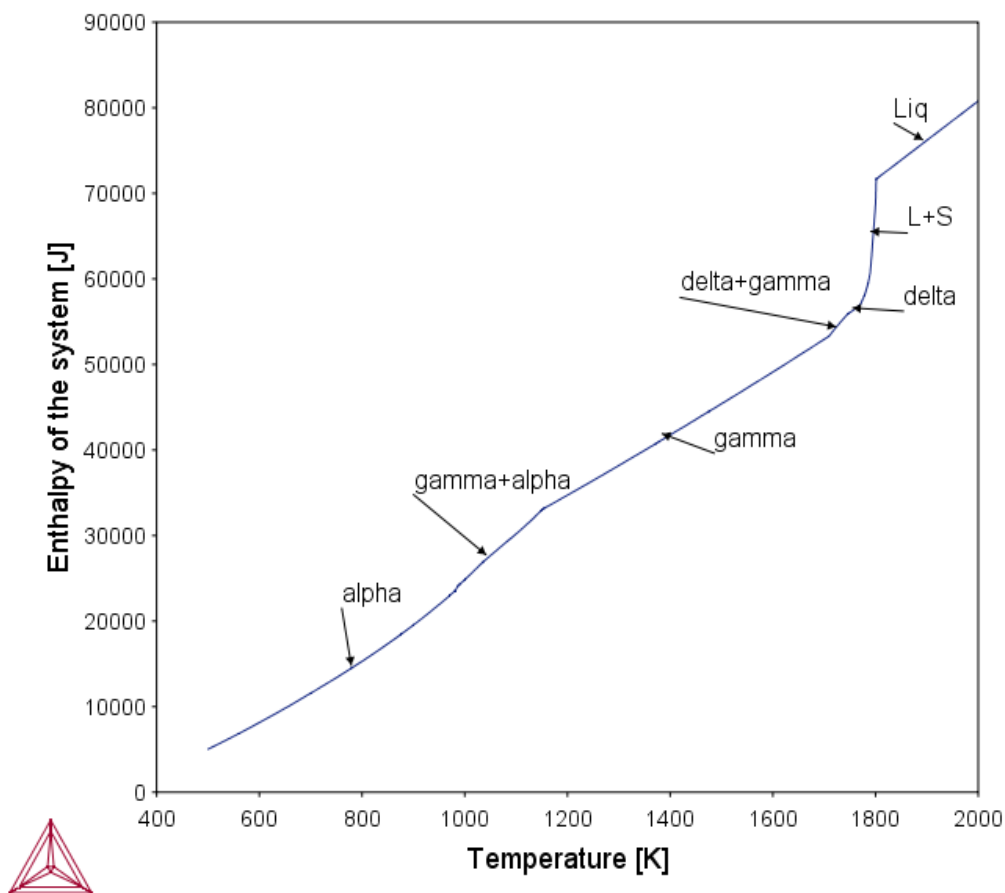

Figure 3.3. Change in enthalpy of micro alloyed steel with temperature

Table 3.1. Chemical composition of micro-alloyed steel

C	Mn	S	P	Si	Al	Ti	N	Nb	V	Ni	Cr	Mo
0.061	0.64	0.005	0.016	0.026	0.05	0.037	0.004	0.021	0.003	0.009	0.01	0.001

33

The lever rule calculations are performed to calculate the phase fraction during solidification. Two phase transformation are considered such as liquid to solid and solid state transformation such as Delta to Gamma and Gamma to Alpha phase change.

$$f_l = 1, \qquad if \ \ T \geq T_{liq}$$

$$f_l = \frac{T - T_{sol}}{T_{sol} - T_{liq}}, \qquad if \ \ T_{sol} \leq T < T_{liq}$$

$$f_l = 0, \qquad if \ T \leq T_{sol}$$

Where f_l is fraction of liquid phase, T_{liq} is liquidus temperature T_{sol} is solidus temperature and T is temperature of steel. In case of solid state transformation, the solidus and liquidus temperatures are replaced by the corresponding phase transformation temperatures (T_{delta}, T_{gamma} and T_{alpha}) to calculate the phase fractions.

3.1.4 Effective thermal conductivity of steel

The effective thermal conductivity of steel is calculated based on temperature, amount of carbon content and phase fraction. The conductivity of each phase at different temperature is calculated based on fitted equations which are obtained from the experimental data[3]. The thermal conductivity of 0.061 percent carbon steel with temperature is shown in Fig (3.4).

$$k_{eff} = f_\alpha k_\alpha + f_\gamma k_\gamma + \ f_\delta k_\delta + f_l k_l \tag{3.4}$$

Where k_{eff} is effective thermal conductivity, k and f is conductivity and fraction of respective phases such as alpha (α), gamma (γ), delta (δ) and liquid (l). The conductivity of each phase are

$k_\alpha = (80.91 - 9.9269 \times 10^{-2}T + 4.613 \ \times \ 10^{-2} \ T^2)(1 - a_1(C_{pct})^{a_2})$

$k_\delta = (20.14 + \ 9.313 \times 10^{-3}T)(1 - a_1(C_{pct})^{a_2})$

$k_\gamma = (21.6 + \ 8.35 \times 10^{-3}T)$

$k_\delta = 39$

Where

$a_1 = (0.425 - 4.385 \times 10^{-4}T)$
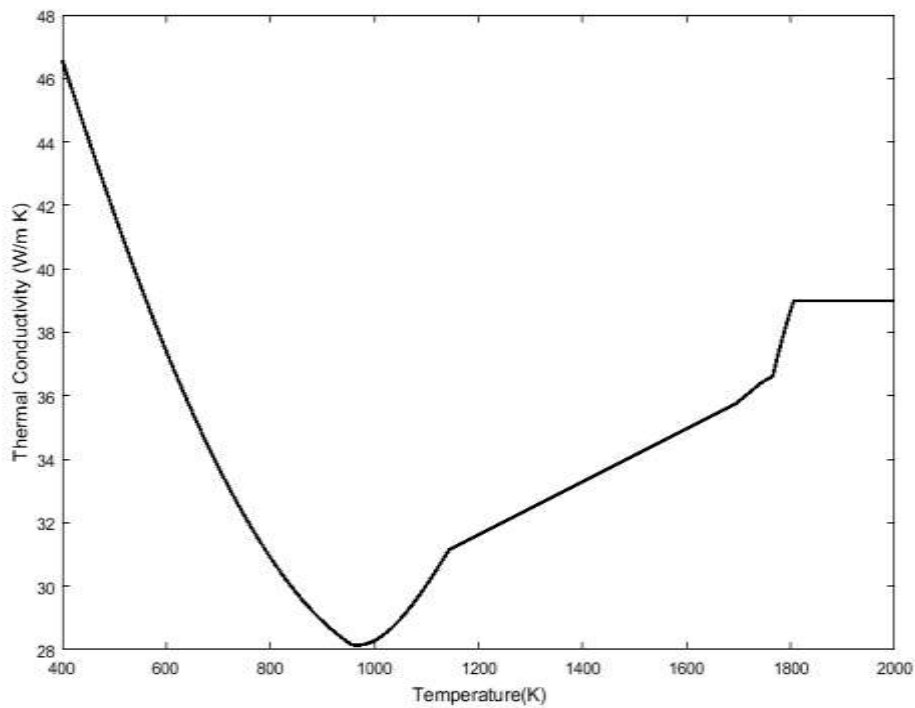
$a_2 = (0.209 + 1.09 \times 10^{-3}T)$

Figure 3.4. The thermal conductivity of 0.061 percent carbon steel

3.1.5 Boundary conditions

(a) Mould region

To solve the governing equation, different boundary conditions are required in mould and secondary cooling region such as spray and roll contact cooling. In mould region, heat transfer coefficient (h_{gap}) is calculated between mould and steel shell below the meniscus. The heat transfer coefficient mainly depends on the resistance offered by the solid and liquid layer of mould slag as shown in Fig (3.5).
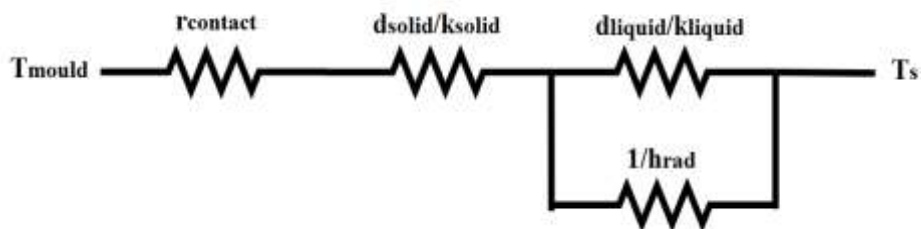

Figure 3.5. Thermal resistance between mould and strand shell surface

35

$$h_{gap} = \cfrac{1}{\left(\left(r_{contact} + \dfrac{d_{solid}}{k_{solid}}\right) + \dfrac{1}{\left(\dfrac{k_{liquid}}{d_{liquid}} + h_{rad}\right)}\right)} \tag{3.5}$$

Where, $r_{contact}$ is contact resistance between the mould and solid slag layer, d_{solid} is thickness of solid slag, d_{liquid} is thickness of liquid slag, k_{solid} is conductivity of solid slag layer and k_{liquid} is conductivity of liquid slag layer. The radiation heat transfer occurs in liquid slag layer which is represented by

$$h_{rad} = \cfrac{m^2 \sigma \left(T_s^2 + T_{fsol}^2\right)\left(T_s + T_{fsol}\right)}{\left(0.75\, a\, d_{liquid}\right) + \dfrac{1}{\varepsilon_{slag}} + \dfrac{1}{\varepsilon_{steel}} - 1} \tag{3.6}$$

Where T_s and T_{fsol} are surface temperature of steel and solidification temperature of mould slag respectively. m and a are refractive index and absorption coefficient of slag. ε_{slag} and ε_{steel} are emissivities of slag and steel respectively.

To calculate heat transfer coefficient in mould region, it is necessary to predict solid and liquid slag layer thickness below the meniscus. Therefore, mass balance is performed based on average mould powder consumption (Q_{slag}) per unit area of strand surface for a given casting speed (V_c) with the flow rate of solid and liquid slag is given by

$$\frac{Q_{slag} \times V_c}{\rho_{slag}} = V_{solid} d_{solid} + V_{liquid} d_{liquid} \tag{3.7}$$

Where ρ_{slag} is the density of slag, V_{solid} is velocity of solid slag layer and V_{liquid} is average velocity of liquid slag.

The velocity of solid slag layer (V_{solid}) is always less than casting speed (V_c) of the strand and depends on input solid slag ratio (F_v).

$$V_{solid} = F_v . V_c \tag{3.8}$$

The velocity of liquid slag is not constant due to change in viscosity (μ_s) corresponding to temperature (T) variation down to the mould which is given by Eqn (3.9). The thickness of the liquid slag is predicted by assuming laminar Couette flow given in Eqn (3.10).

$$\mu_s = \mu_o \left(\frac{T_o - T_{fsol}}{T - T_{fsol}} \right)^n \tag{3.9}$$

Where, n is a constant used to fit measured data and μ_o is viscosity of slag at reference temperature T_o.

$$\frac{\partial}{\partial x} \left(\mu_s \frac{\partial V_{liquid}}{\partial x} \right) = \left(\rho_{steel} - \rho_{slag} \right) g \tag{3.10}$$

Where the flow of liquid slag is opposed by the difference between ferro-static pressure of liquid steel and weight of slag. The average velocity of liquid slag (V_{liquid}) is obtained by integrating Eqn (3.10) across the liquid slag region as shown in Fig (3.6) and given by Eqn (3.11)

$$V_{liquid} = \frac{\left(\rho_{steel} - \rho_{slag} \right) g d_{liquid}^2}{\mu_s (n+2)^2 (n+3)} + \frac{V_c + V_{solid}(n+1)}{(n+2)} \tag{3.11}$$
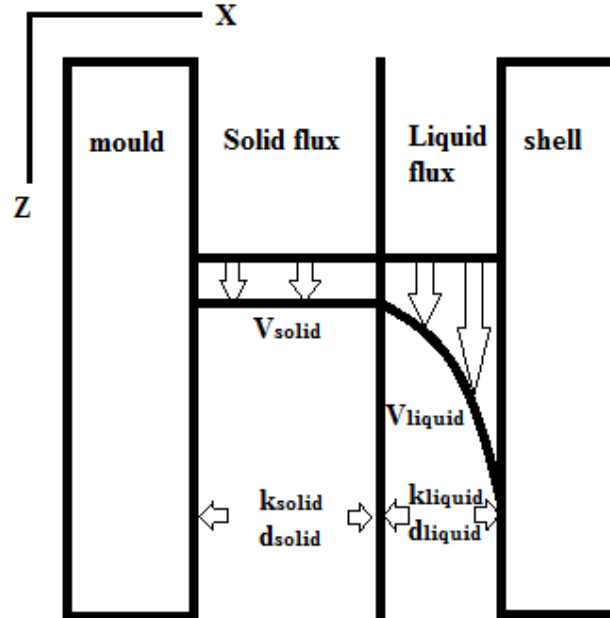

Figure 3.6. Velocity profile of solid and liquid slag layer.

(b) Secondary cooling region

Heat transfer mechanism in secondary cooling zone occurs by convection through spray cooling, radiation, conduction in roll contact region and natural convection as shown in Fig (3.7).

In case of spray cooling, the strand is cooled by the combination of pure water spray and air water mixture (air-mist). Hence, in both cases, the heat transfer coefficient is directly related to water flux. However, the heat transfer coefficient of pure water spray (h_{spray}) is described by Eqn (3.12) which has been successfully used by other modellers [3][8].

$$h_{spray} = A \times Q_{water}^c \times (1 - b \times T_{spray}) \qquad (3.12)$$

Where A =0.3925, b =0.0075, c = 0.55, Q_{water} is water flux (L/m²s) and T_{spray} is temperature of spray water.
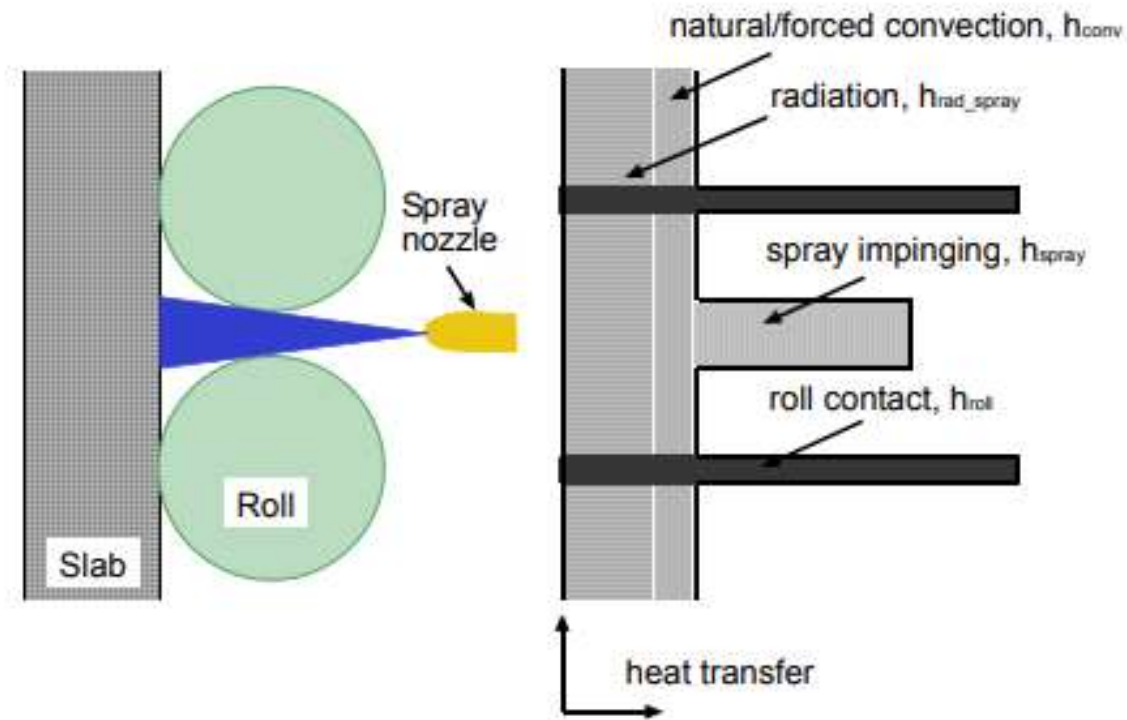

Figure 3.7. Schematic of secondary cooling zone region[3]

Heat transfer coefficient of air-water spray is given by Eqn (3.13) which is obtained from Kaestle et al[9]. It is observed that heat transfer coefficient of air-water spray is 1.7-2 times more than pure water spray.

$$h_{air-water\,spray} = 0.35\,Q_{water} + 0.13 \qquad (3.13)$$

However, the spray nozzles and water flow rate details are required to calculate the water flux. The flow rate in different cooling zones and the corresponding number of nozzle for SMS DEMAG machine is reported in Table (3.2).

Table 3.2.Details of water flow rate and number of nozzles with respective cooling zone

Cooling Zone	Number of Nozzles	Water Flow Rate (LPM)
Below to the mould	7	105.5
Segment 0 (I)	18	181
Segment 0 (II)	21	127
Segment 1+2	11	145
Segment 3+4	10	106
Segment 5+6	10	85
Segment 7+8+9	15	95
Segment 10+11+12	15	55
Segment 13+14+15	15	62

The radiation heat transfer [3] is governed by

$$h_{rad} = \sigma \times \varepsilon_{steel}(T_s^2 + T_{amb}^2)(T_s + T_{amb}) \qquad (3.14)$$

Where T_s is strand surface temperature and T_{amb} is ambient temperature.

The heat transfer through the roll contact is calculated based on the fraction of heat extracted (f_{roll}) by the rolls [3].

$$h_{roll} = \frac{f_{roll}}{L_{roll\,contact}(1 - f_{roll})}\Big[(h_{rad} + h_{conv} + h_{spray})L_{spray} \\ + (h_{rad} + h_{conv})\big(L_{spray\,pitch} - L_{spray} - L_{roll\,contact}\big)\Big] \qquad (3.15)$$

Where, L_{spray} is spray length, $L_{spray\,pitch}$ is the length between end of roll contact to next roll contact beginning and $L_{roll\,contact}$ is contact length of rolls on strand surface. The contact length of roll on strand surface is calculated based on the contact angle of roll and diameter of rolls in each segment is given in Table (3.3).

The heat transfer coefficient of natural convection (h_{conv}) is very small which is assumed as 8.7 W/m^{2}K.

Table 3.3. Details of roll diameter in each segment of casting machine

Segment Number	No of rolls	Roll Diameter (mm)
Segment 0 (I)	8	130
Segment 0 (II)	5	160
Segment 1	6	215
Segment 2-3	10	255
Segment 4-5	10	290
Segment 6-7	10	310
Segment 8-15	40	325

3.2 Equilibrium precipitation model

Thermo-Calc simulation software is performed to find out the precipitation phase at equilibrium for a micro alloyed steel composition as given in Table 3.1. Simulation is performed in console mode. This starts with system utility where steels/Fe-alloys v8.1 (TCFE8) and steel/Fe-alloys mobility v3.0 (MOBFE3) mobility database has been selected and elements needed for thermodynamic calculation is obtained. The thermochemical properties of selected elements are collected from the database and passed to Gibbs energy minimizer function i.e. POLY-3 to calculate equilibrium phases at a given temperature. By taking calculated phases as a reference state, stepping calculation has been performed over a temperature range and results are plotted. Figure (3.8) shows the flow chart of Thermo-calc simulation.
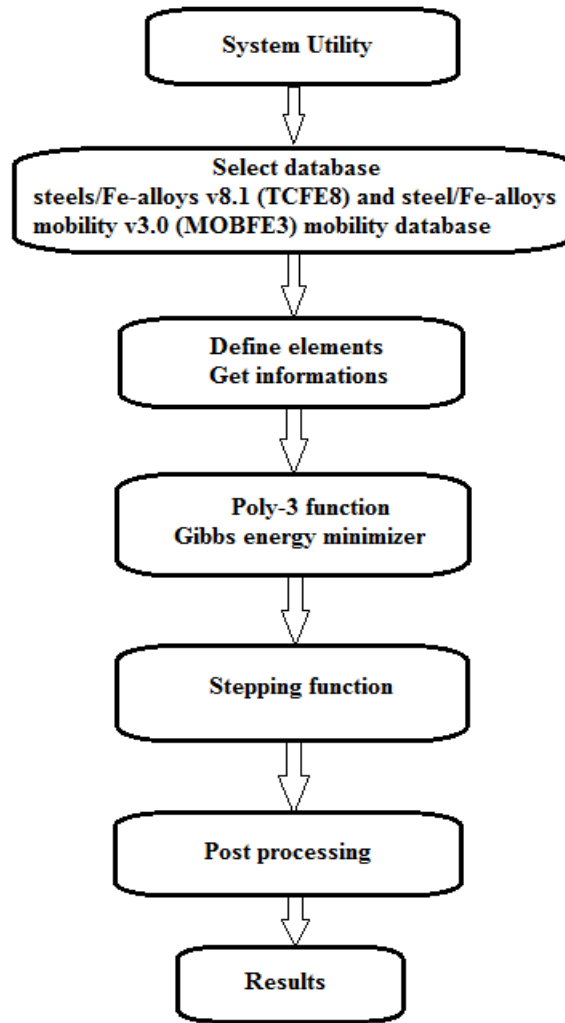
Figure 3.8. Flow chart of Thermo-Calc simulation

3.3. Non-equilibrium precipitation model

For non-equilibrium precipitation calculations, TC-PRISMA has been used and calculations are performed in the graphical user interface. Steels/Fe-alloys v8.1 (TCFE8) and steel/Fe-alloys mobility v3.0 (MOBFE3) mobility database are used and information of selected elements are obtained. Subsequently, the precipitate calculator has been used where simulation conditions such as precipitate phase, matrix phase, simulation time and thermal history and nucleation properties such as nucleation sites and microstructure information and parameters such as interfacial energy and volume data's are entered. Finally, simulation is performed and results are plotted.
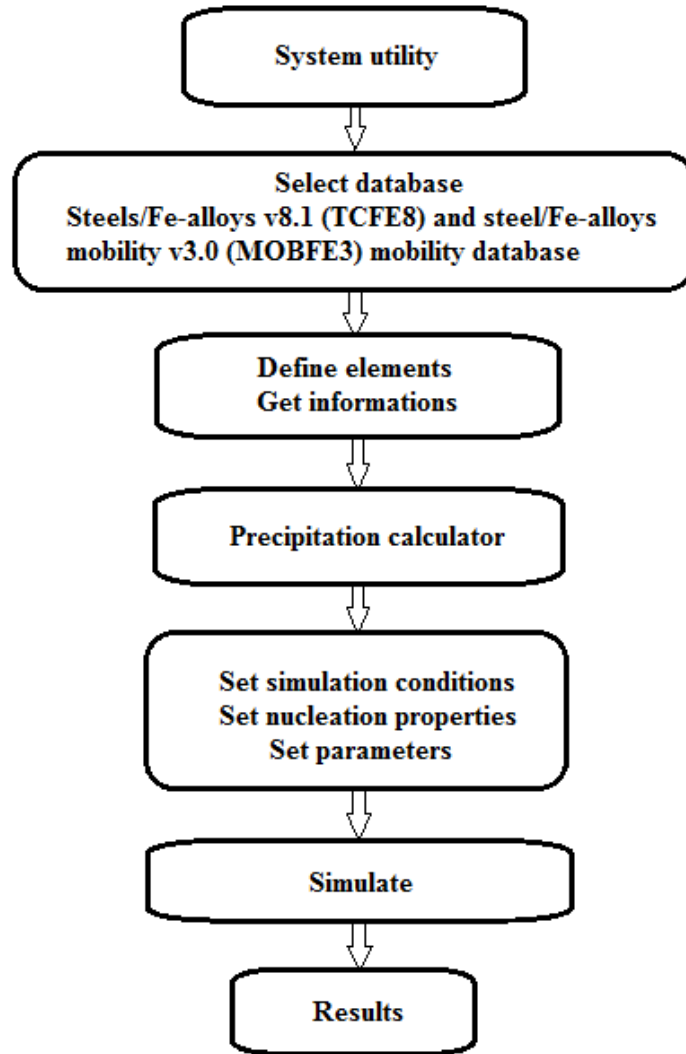
Figure 3.9. Flow chart of TC-PRISMA simulation

3.4 Solution Methodology

The 1-D heat conduction model by enthalpy method starts with initialling casting speed, carbon content and pouring temperature of molten steel. The linear expressions obtained from the enthalpy plot are solved to calculate the phase transformation temperature. The position of the strand is continuously calculated at a given casting speed based on that the corresponding heat transfer coefficient is evaluated. In mould region, assumed mould temperature is taken as an input for the model and with help of heat and mass balance the thickness of solid and liquid mould flux has been evaluated. However in the initial stage with known pouring temperature the initial enthalpy, phase fraction and effective thermal conductivity (k_{eff}) are calculated. The discretised equations are solved in each time step (Δt)

42

by using a simple explicit scheme to calculate the new enthalpy (H^{new}) based on the evaluated properties of previous time step and the temperature is back calculated from evaluated new enthalpy by using this T=T(H) expression. The input conditions of the model are given in table (3.4). Parallel to this, the equilibrium thermodynamic calculation has been performed independently by using Thermo-Calc for a given steel composition of micro alloyed steel and different types of precipitates have been analysed. Finally, the predicted strand temperature history from the 1-D heat conduction model is used for non-equilibrium precipitate calculation in TC-PRISMA where mean particle radius and matrix composition are simulated. Figure (3.10) shows the flow chart of 1-D heat conduction model parallel with equilibrium (Thermo-Calc) and non-equilibrium (TC-PRISMA) simulation.

Table 3.4. Simulation input conditions

|		
Carbon content	0.061	percent
Liquidus temperature T_{liq}	1801	K
Solidus temperature T_{sol}	1769	K
Steel density ρ_{steel}	7400	kg/m^3
Steel emissivity ε_{steel}	0.8	-
Mould powder solidification temperature T_{fsol}	1318	K
Liquid mould slag conductivity k_{liquid}	1.5	W/mK
Solid mould slag conductivity k_{solid}	1.5	W/mK
Contact resistance between mould and slag $r_{contact}$	5.0×10^{-9}	m^{2}K/W
Reference viscosity at 1573 K μ_o	1.1	Poise
Exponent at reference viscosity n	0.85	-
Slag density ρ_{slag}	2500	kg/m^3
Slag absorption factor a	250	m^{-1}
Slag refractive index m	1.5	-
Slag emissivity ε_{slag}	0.9	-
Mould powder consumption rate Q_{slag}	0.6	kg/m^2
Solid slag speed factor F_v	0.175	-
Casting speed V_c	1.5	m/min
Pour temperature T_{pour}	1821	K
Slab geometry W×T	1300×220	mm×mm
Working mould length Z_{mould}	800	mm
Spray water temperature T_{spray}	303	K
Spray nozzle length L_{spray}	50	mm
Roll contact angle	7	deg
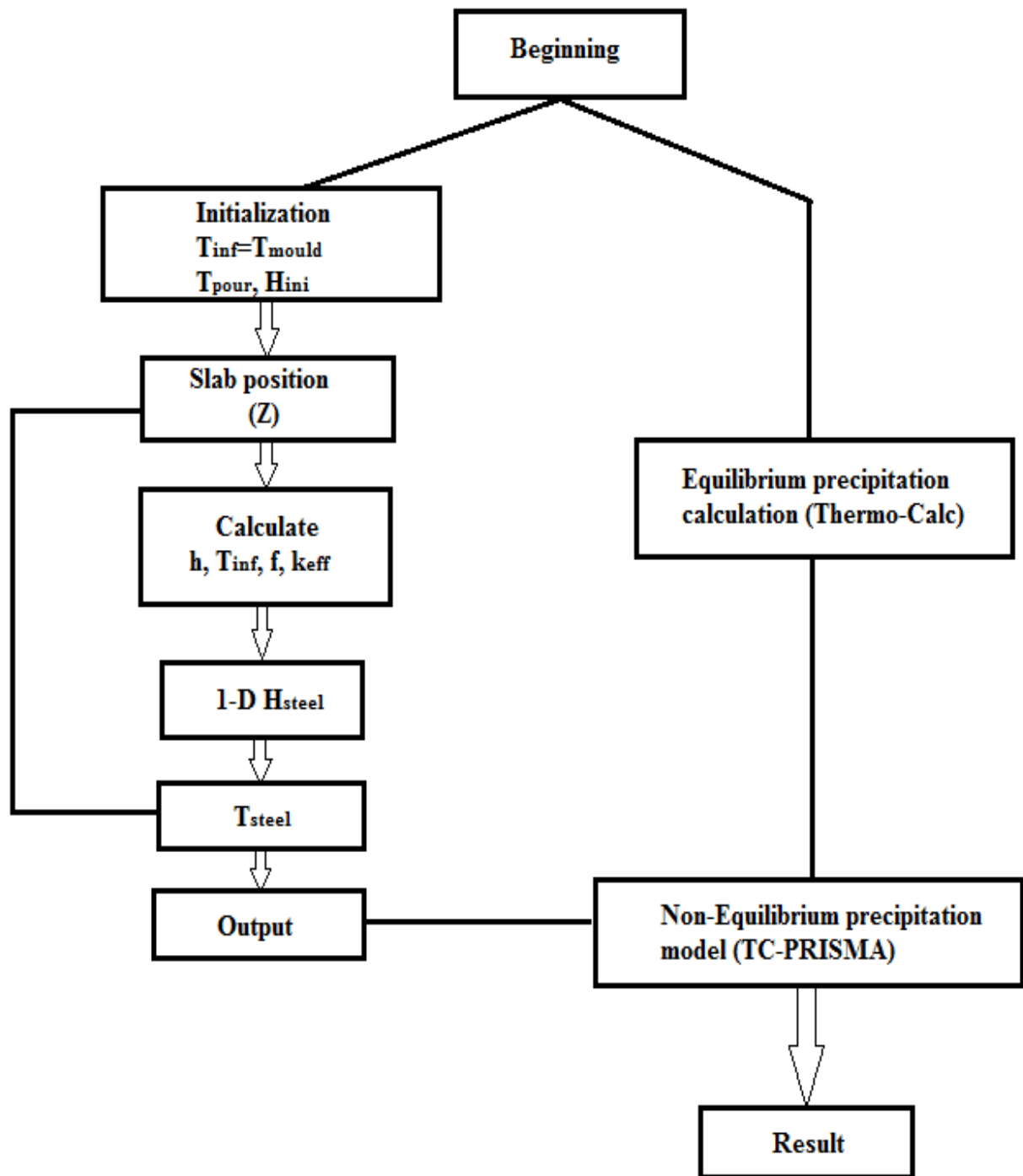
Figure 3.10. flow chart of 1-D heat conduction model with equilibrium and non-equilibrium simulation.

CHAPTER: 4 Model validation

Calculation of Shell thickness based on the temperature distribution in the strand is one of the important parameter obtained by this model. Grid independent study has been done to observe the effect of grid size on the accuracy of this parameter which leads to reduction in computational time without compromising the accuracy of the solution. In the current domain, the shell thickness at exit of the mould during solidification is studied with various grid sizes (number of nodes) as shown in Fig (4.1).
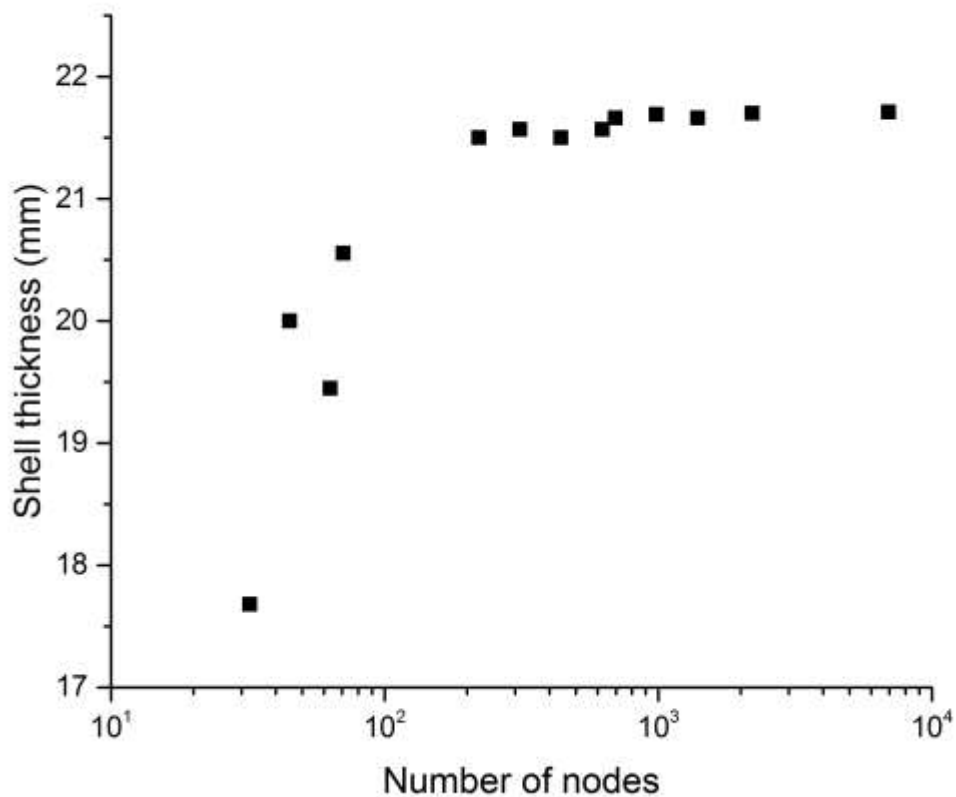
Figure 4.1. Effect of grid size on shell thickness

It is observed that the variation in the shell thickness as the number of node point increases and variation become minimal after reaching the certain number of nodes. Hence node number of 985 is chosen as grid independent study for further simulation and time step of 0.0002 seconds is also calculated by fixing dimensionless courant number.

In order to validate the result of 1-D transient heat conduction model by enthalpy method, the calculated shell thickness of 0.044% plain carbon steel is compared with the CON1D model by Thomas et al [3] as shown in Fig(4.2). The input conditions are taken for this simulation is same as used by Thomas et al as given in Table (4.1).

Table 4.1. Input conditions for model validation

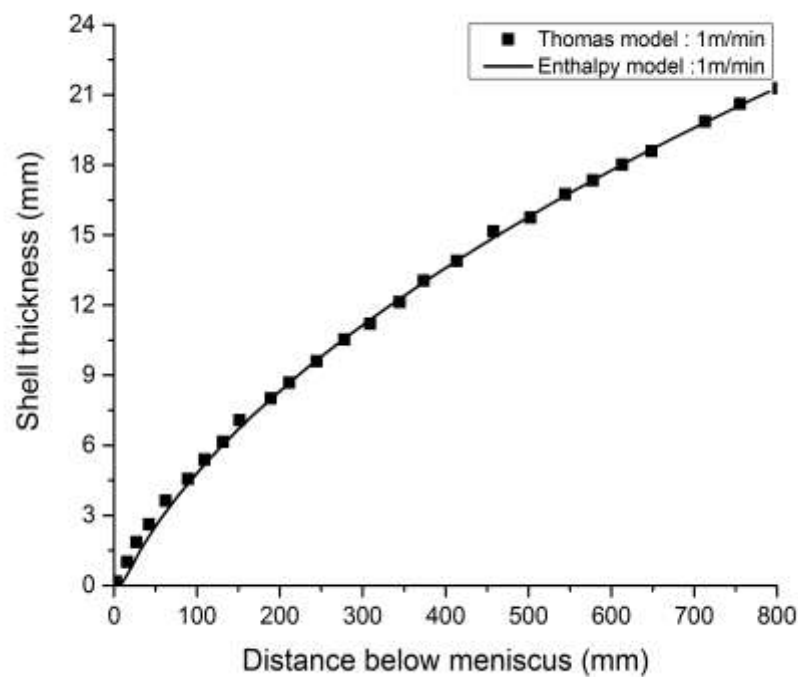| Carbon content	0.044%
Pour temperature	1550 °C
Liquidus temperature	1529 °C
Solidus temperature	1509 °C
Casting speed	1 m/min
Working mould length	800 mm

Figure 4.2. Comparing shell thickness of enthalpy model with Thomas model

It can be clearly seen that the trend and calculated value of shell growth in the mould of 800 mm contact length and casting speed of 1m/min is perfectly matching which makes sure that the enthalpy way of calculation is working well.

46

CHAPTER: 5 Results and discussion

5.1 Temperature distribution

The temperature distribution of the strand is one of the main parameters calculated by this model. Based on this, other parameters such as shell thickness and metallurgical length can be generated. This simulation has been done for 29.2225 meters begins from meniscus to last roll of casting machine. Figure (5.1) shows the predicted temperature of strand surface in the mould region at 1.5m/min casting speed. It is observed that gradual decrease in surface temperature due to continuous heat extracted by water cooled copper mould. This surface temperature is not only influenced by mould temperature and also depends on the mould flux properties between mould and strand surface; corresponding thickness of liquid and solid mould flux layer which give resistance to heat transfer.
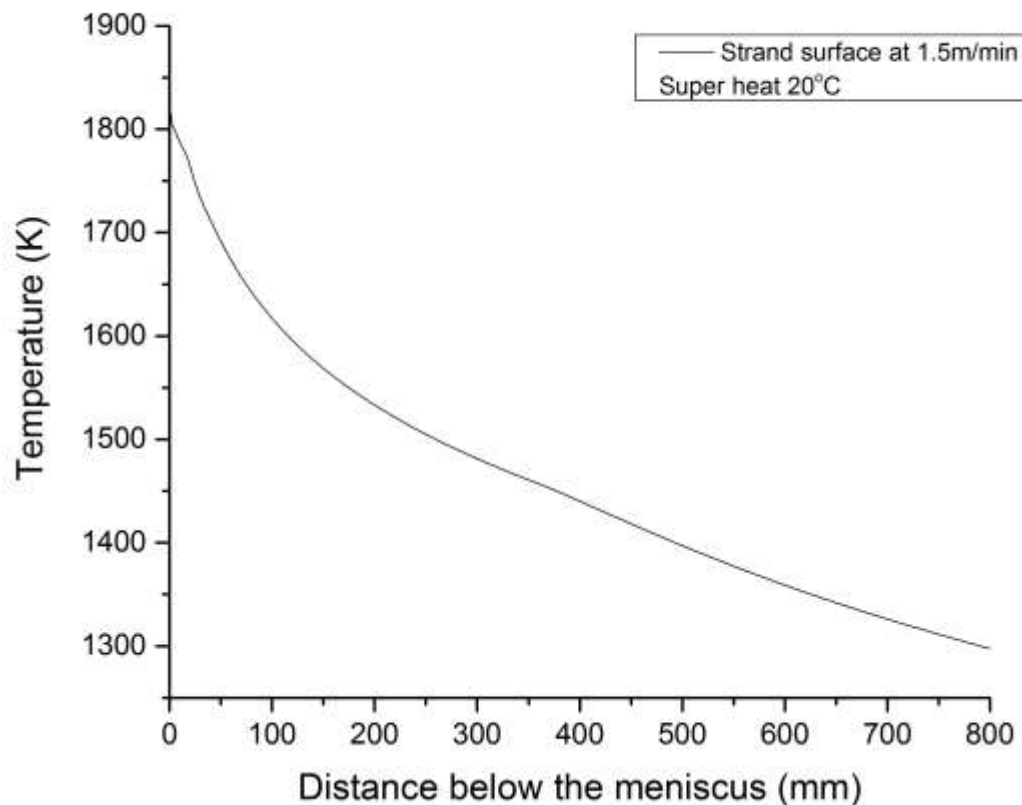

Figure 5.1. The Surface temperature of strand at 1.5m/min in mould region

Figure (5.2) shows the surface temperature of strand till 10 meter of machine length. It is known that the heat flux is directly proportional to the heat transfer coefficient. The calculated heat transfer coefficient is higher in the case of spray cooling region followed by roll contact. Therefore the temperature of the strand continuously fluctuates due to the different cooling rate in the secondary cooling zone and convective heat transfer of molten steel from inside. However, in roll contact region the heat flux is a function of the fraction of heat extracted by rolls where 0.05 is used for roll diameter of less than 200 mm and rest of that 0.2 has been used. Therefore the temperature drop is not observed near mould region because of using small rolls but after 3.15 meters machine length temperature drop has been observed between spray cooling regions. It is also noted that the average temperature fluctuation along casting direction is within 100K which is one of the important criteria is needed especially to save longitudinal and transverse crack formation on the surface.
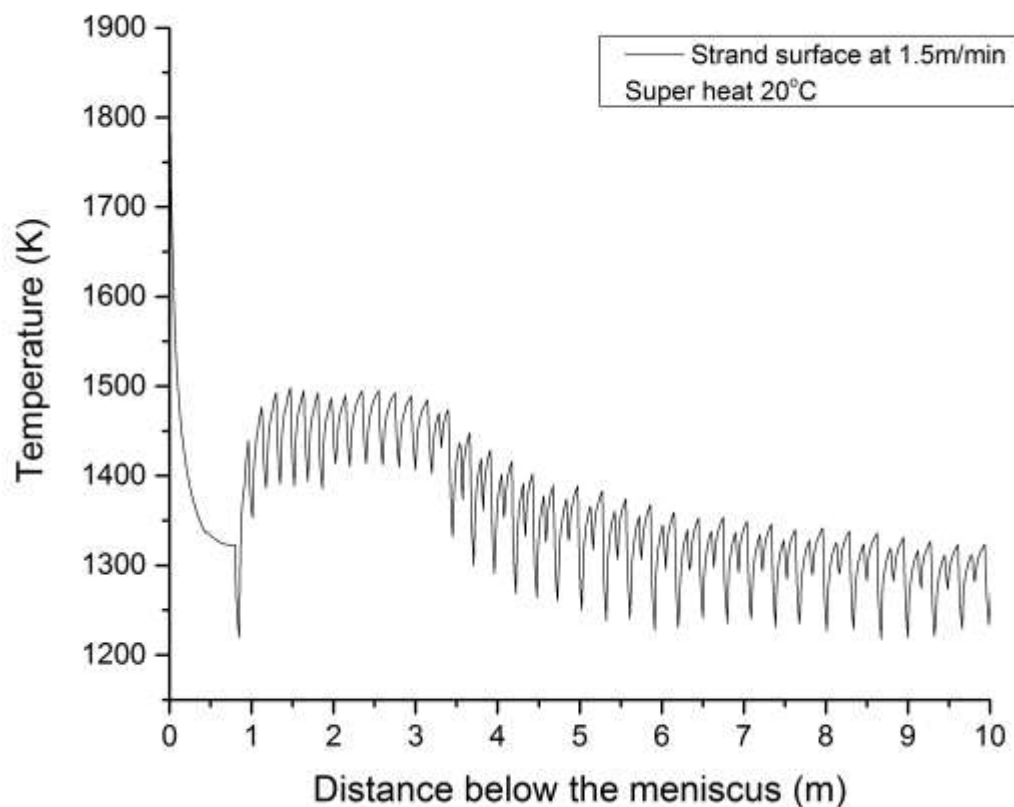

Figure 5.2. The surface temperature of strand at 1.5m/min till 10m machine length

Figure (5.3) shows the strand surface and internal temperature history of complete machine length. A difference in temperature fluctuation pattern has been observed before and after 3.3 meter of machine length. The reason for the difference is using pure water spray cooling before 3.3 meters and air water (air-mist) cooling is used after that. However, it is well known that, the heat extraction by air-mist cooling is higher than pure water spray cooling which leads to higher temperature drop after 3.3 meter machine length. Surface and subsurface of the strand undergoes high temperature fluctuation due to the heat extraction at the surface and reheating of molten steel. However, at about 20mm depth from the surface, the fluctuations have almost become damped out.
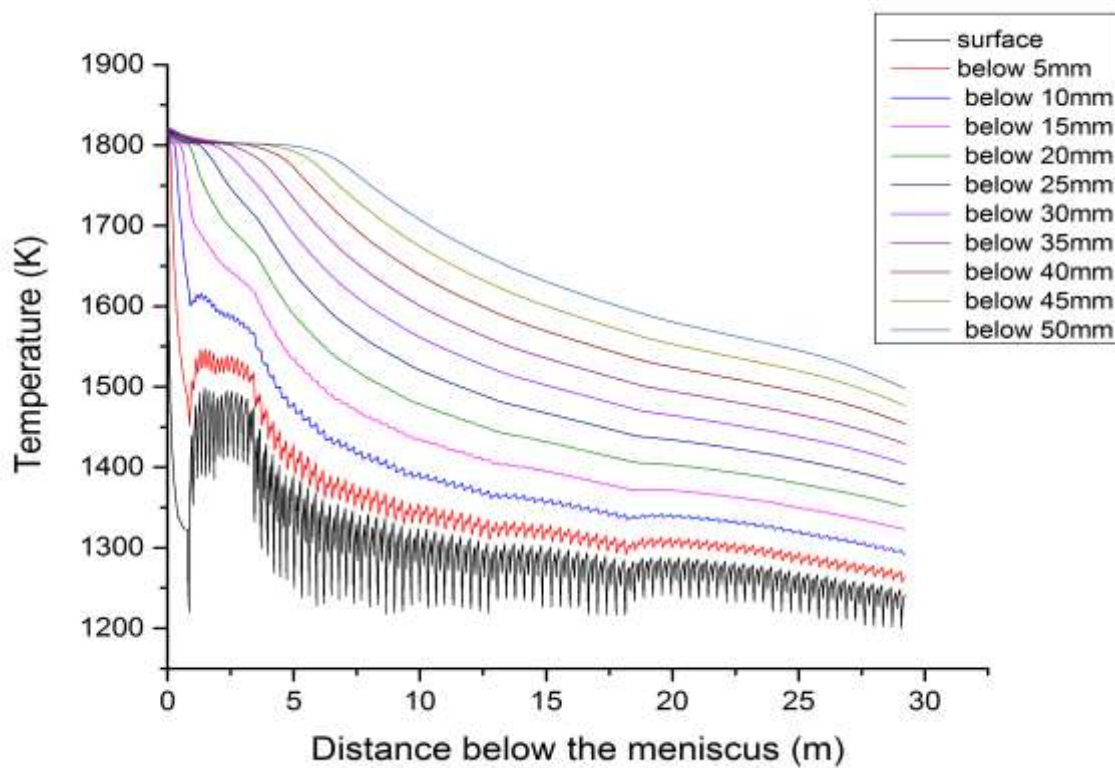

Figure 5.3. Internal temperature history of the strand

5.2 Shell thickness

Shell thickness is another important parameter calculated based on tracking the fraction of solid phase. Shell formation during continuous casting has received considerable attention as formed shell should be sufficiently thick to withstand ferro-static pressure given by the molten steel. Figure (5.4) shows the predicted shell growth of 800mm mould contact

49

length at 1.5m/min casting speed and 20 °C super heat. Hence, the predicted shell thickness at mould exit is 16.10mm.
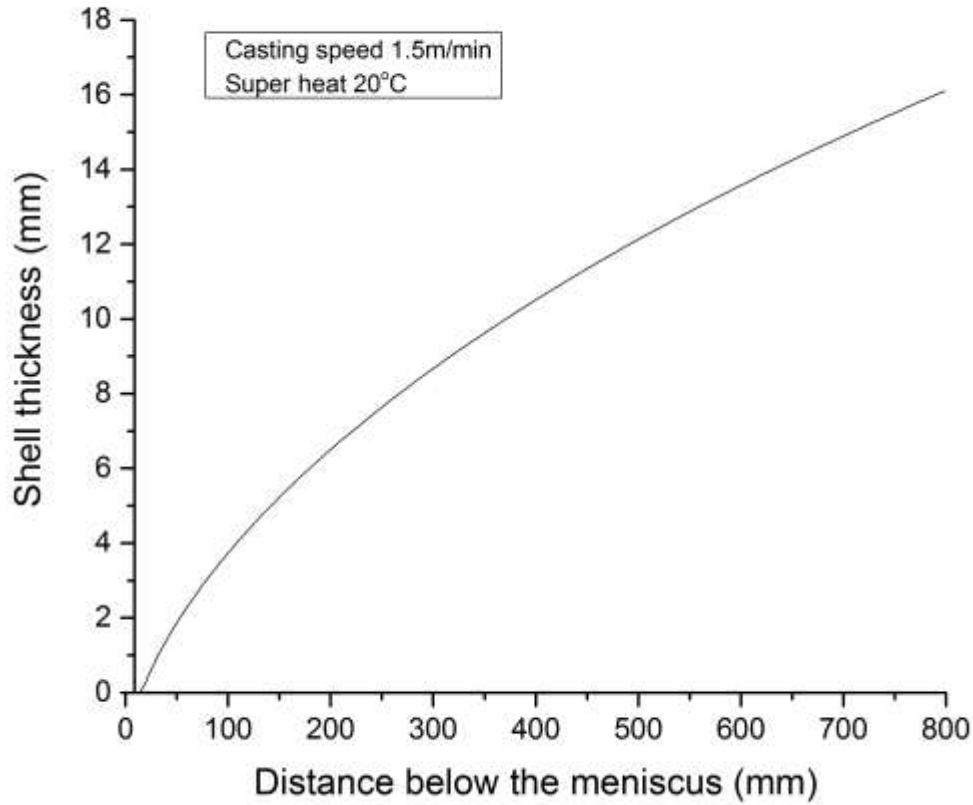

Figure 5.4. Predicted shell thickness at 1.5m/min casting speed

5.3 Parametric studies

5.3.1 Effect of casting speed on temperature distribution and shell thickness

The temperature distribution and shell thickness is greatly influenced by casting speed of strand and super heat of molten steel. The model has been simulated at different casting speed such as 1.1, 1.3 and 1.5m/min. Figure (5.5) shows temperature distribution of strand with these casting speeds with the fixed super heat of 20 °C in the mould region. The temperature of the strand at mould exit for lower casting speed is lesser than casting strand at higher speed. This is due to the difference in the residence time of strand in the mould results in higher heat extraction. The calculated residence time at 1.1, 1.3 and 1.5m/min are 43.63,

36.92 and 32 seconds respectively. Similarly, the predicted shell thickness at 1.1, 1.3 and 1.5m/min is 19.902 mm, 17.778 mm and 16.101mm respectively. Therefore, the shell growth according to the temperature drop is directly proportional to the residence time of strand in the mould region.
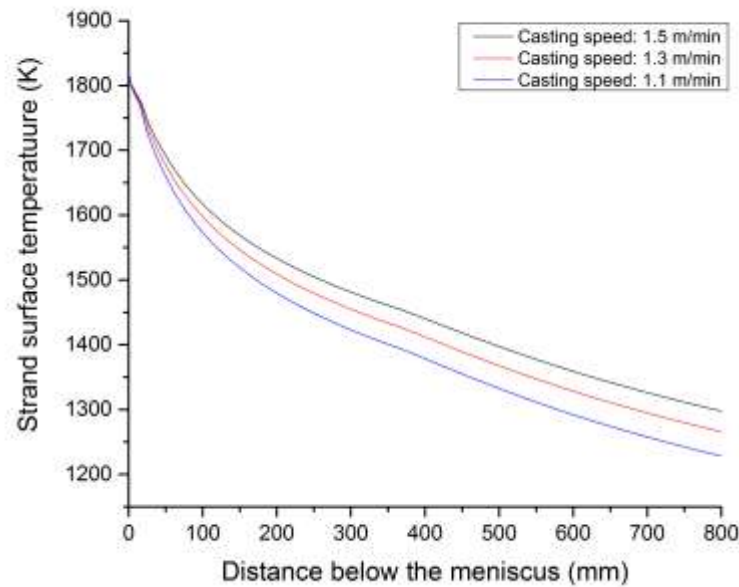

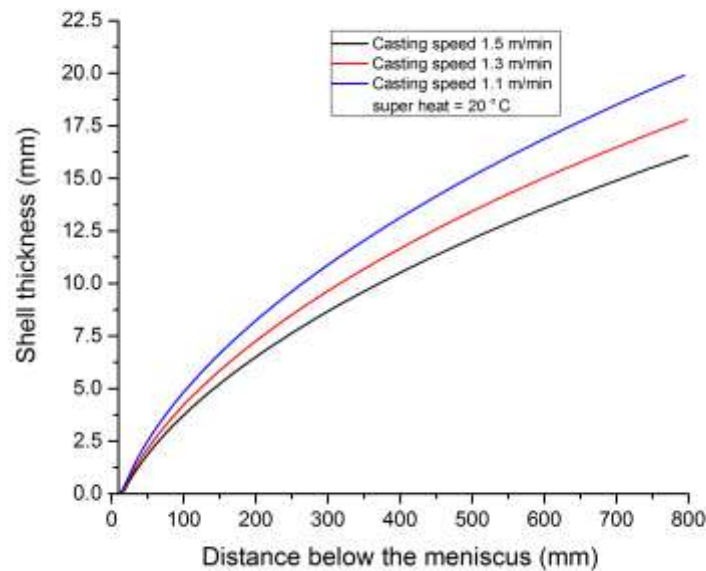Figure 5.5. Comparison of strand surface temperature at the different casting speed.

Figure 5.6. Comparison of shell thickness at 1.1, 1.3 and 1.5m/min casting speed

51

5.3.2 Effect of superheat on shell thickness at different casting speed

The shell thickness is evaluated for different super heat of molten steel and casting speed as shown in Fig (5.7). The simulation has been performed in the range of 15°C to 45°C with a super heat interval of 5°C. At 15°C super heat, higher shell growth has been observed at 1.1, 1.3 and 1.5m/min casting speed where shell growth linearly decreases with increasing super heat. Hence, this causes delays of the initial solidification directly at the meniscus so that the first solid forms somewhat below the meniscus and it decreases the rate of shell growth in the upper part of the strand. However, the super heat cannot be decided only by considering the shell thickness; there are other parameters like holding time of molten steel in ladle and tundish has to be considered to select optimum super heat to the casting process.
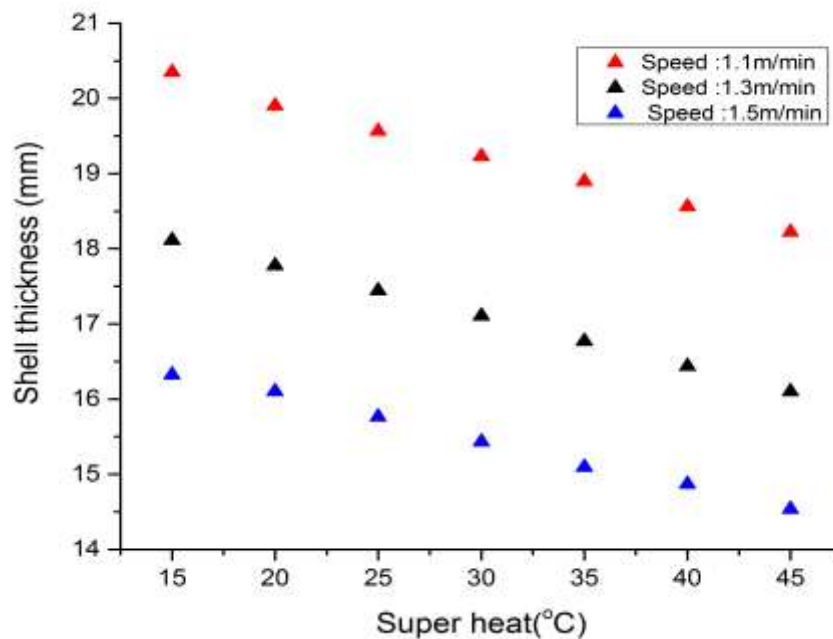

Figure 5.7. The effect of super heat on shell thickness at different casting speed

5.4 Metallurgical Length

Metallurgical length is defined as the length from the meniscus at which the strand becomes completely solid. Figure (5.8) illustrates the temperature distribution of the strand from where the solid and liquid fractions can be calculated by this model. The predicted metallurgical length is 24.725 meter at 1.5m/min casting speed for 29.2225 meters machine length. Much importance has been given to this because the presence of molten steel inside

52

the strand should not exceed the machine length and torch cut off point; if it so the strand may bulge or the molten steel may be drained out of strand completely.
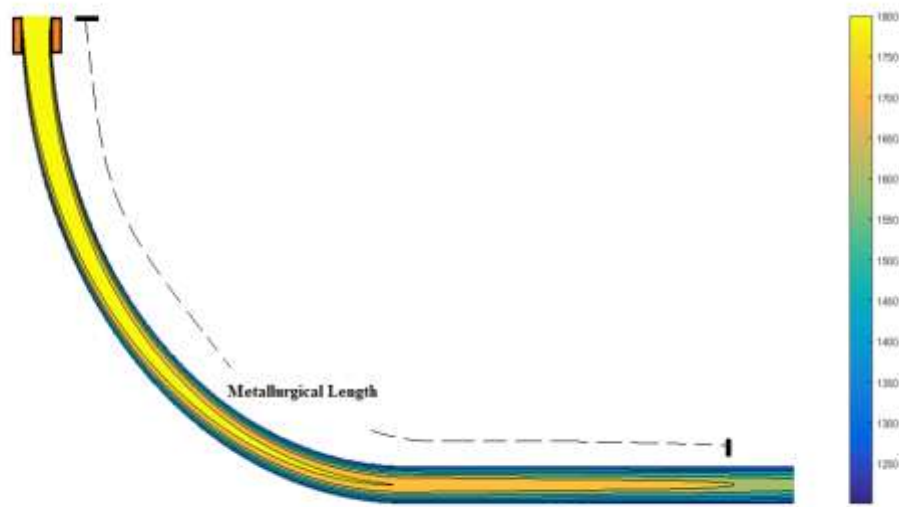

Figure5.8. Diagram illustrating temperature distribution and metallurgical length

5.5 Precipitation at equilibrium

The formation of the precipitate at equilibrium is predicted by using Thermo-Calc simulation software for a micro alloyed steel composition as given in Table (3.1). The amount of all phases as a function of temperature is plotted as shown in Fig (5.9). From this result, except matrix phases, it can be seen that there are individual and complex carbo-nitrides precipitates are forming such as Ti4C2S2, Ti(C,N), MNS and (Nb,Ti)C in the temperature of 1775K, 1769K, 1397K and 1360K respectively. According to the thermodynamics, the solubility product of $Ti_4C_2S_2$ and Ti(C,N) precipitates is much lower than other two precipitates results in presence of this phases at higher temperature.

Moreover, during the continuous casting process, the average temperature of the strand lies above 1300K. Therefore, emphasizes are given to the stable high temperature precipitates. $Ti_4C_2S_2$ precipitate dissolves at 1389K since it is highly soluble in austenite phase but the amount of Ti(C,N) precipitate increases continuously and stable with decreasing temperature. Therefore Ti(C,N) precipitate has been considered to analyse precipitation growth in continuous casting non-isothermal condition. For that, the site fraction of Ti(C,N) precipitate has been analysed with temperature as given in Fig (5.10). According to the mutual solubility

of TiC and TiN, it is reported that the fraction of carbon increases and nitrogen decreases with decreasing temperature.
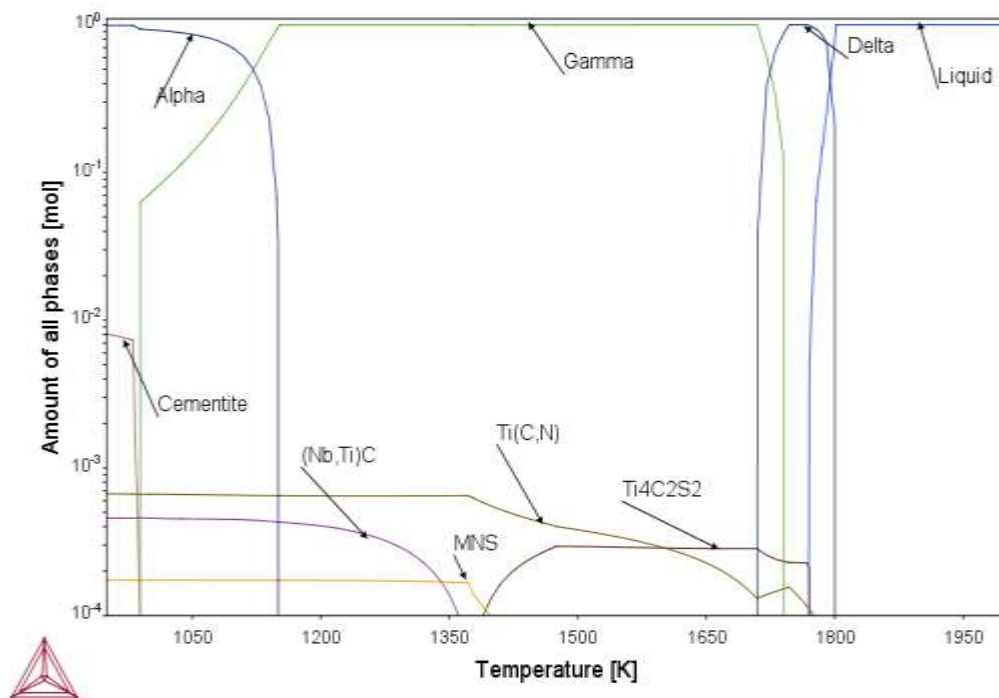

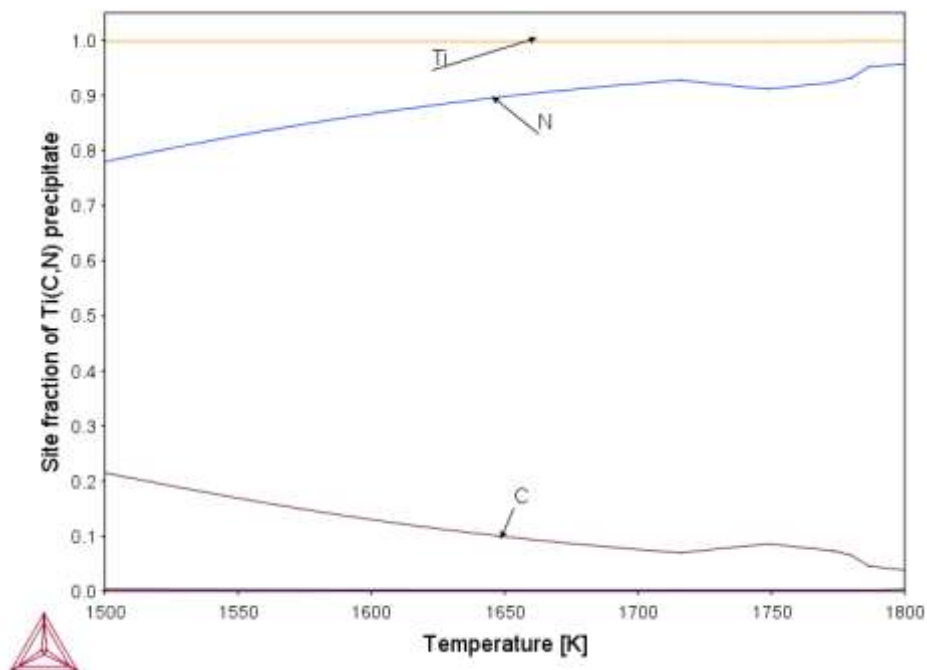Figure 5.9. Amount of all phases with respect to temperature

Figure 5.10. Site fraction of titanium carbo-nitride precipitate

5.6 Non-Equilibrium precipitation

The growth of titanium carbo-nitride (Ti(C,N)) precipitate has been analysed by using TC-PRISMA simulation software in three different location such as 10mm, 20mm and 40mm from the strand surface as shown in Fig (5.11). The obtained thermal history at 1.5m/min casting speed from 1-D heat conduction model has been used as input for this simulation. The calculation is started from the liquid as a matrix phase followed by solid state transformation. It is assumed that the interfacial energy of titanium carbon-nitride is 0.1 J/m^2 and grain boundaries are the only nucleation sites. The predicted mean particle radius with temperature as a function of time and matrix composition of 10mm, 20mm and 40mm location is reported in Fig (5.11), (5.12) and (5.13).
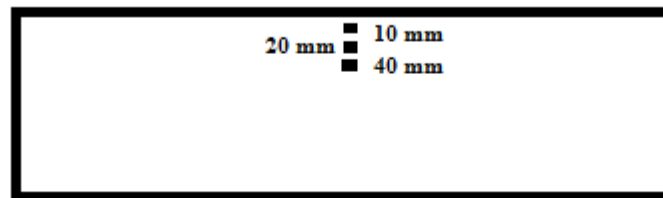

Figure 5.11. Selected location of the strand for precipitate calculation

There are several important points that can be observed from the assembled data

(i) The calculated mean particle radius at 10mm, 20mm and 40mm are 224.02nm, 514.26nm and 825.66nm respectively where at 40 mm, precipitate grows continuously even after casting time of 1165 seconds.

(ii) It is observed that the time taken for precipitation is less than a second and grows gradually in 20mm and 40mm strand location, but in case of 10mm, the strand undergoes high thermal fluctuation correspondingly the precipitation grows and partially dissolve leads to fluctuation in mean particle radius and titanium and nitrogen matrix composition.

(iii) The amount of titanium and nitrogen in matrix continuously decreases as precipitate grows in all there location; there should be a drop in carbon amount in the matrix composition i.e. increase in carbon fraction in precipitate with decreasing temperature which is not observed in non-equilibrium condition. Therefore for a given chemical composition of micro alloyed steel, TiN is more likely to form rather than Ti(C,N) since the cooling rate does not provide time to satisfy the solubility product of TiC in non-equilibrium condition.
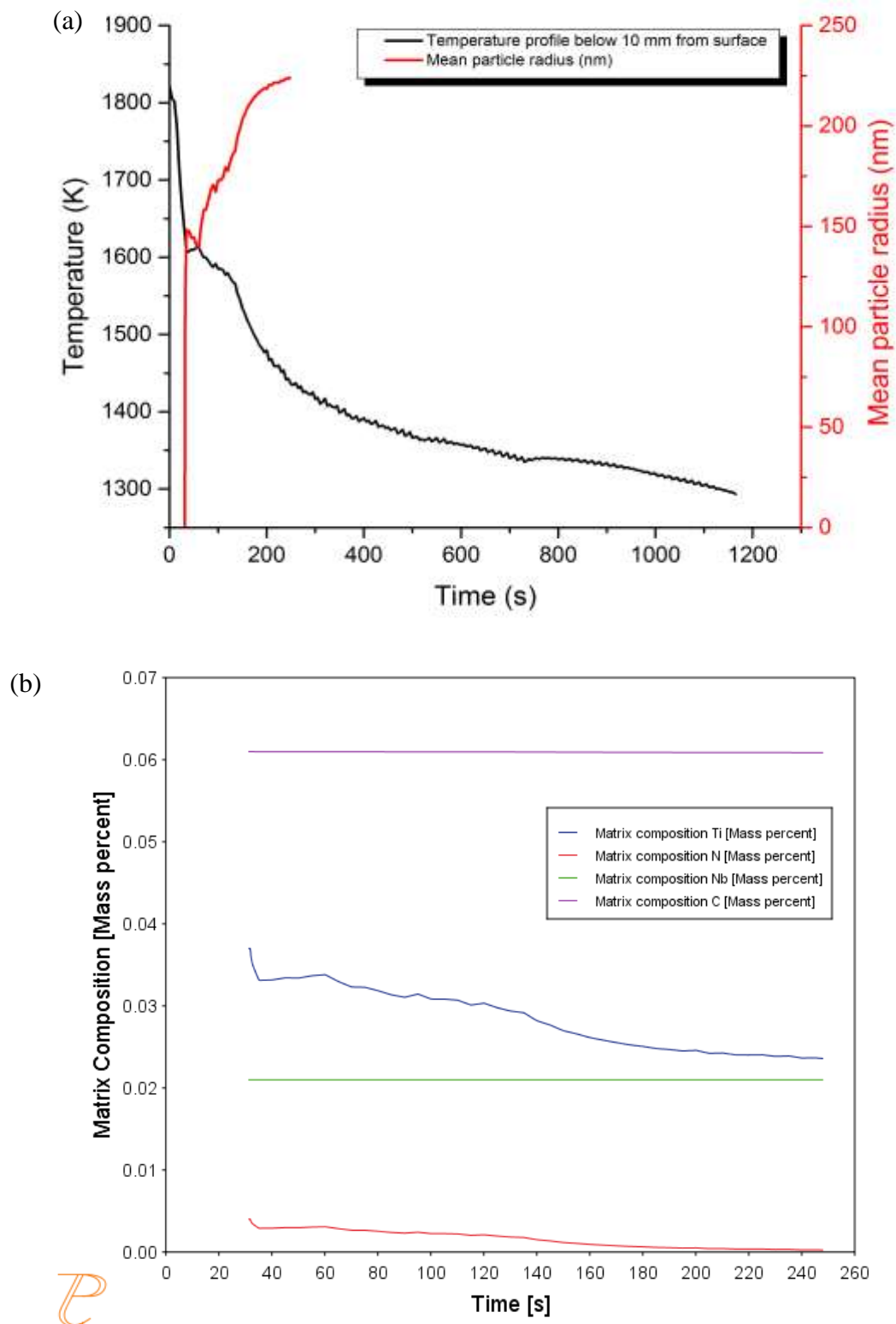
Figure 5.11. Predicted (a) mean particle radius (b) matrix composition at 10 mm below the strand surface
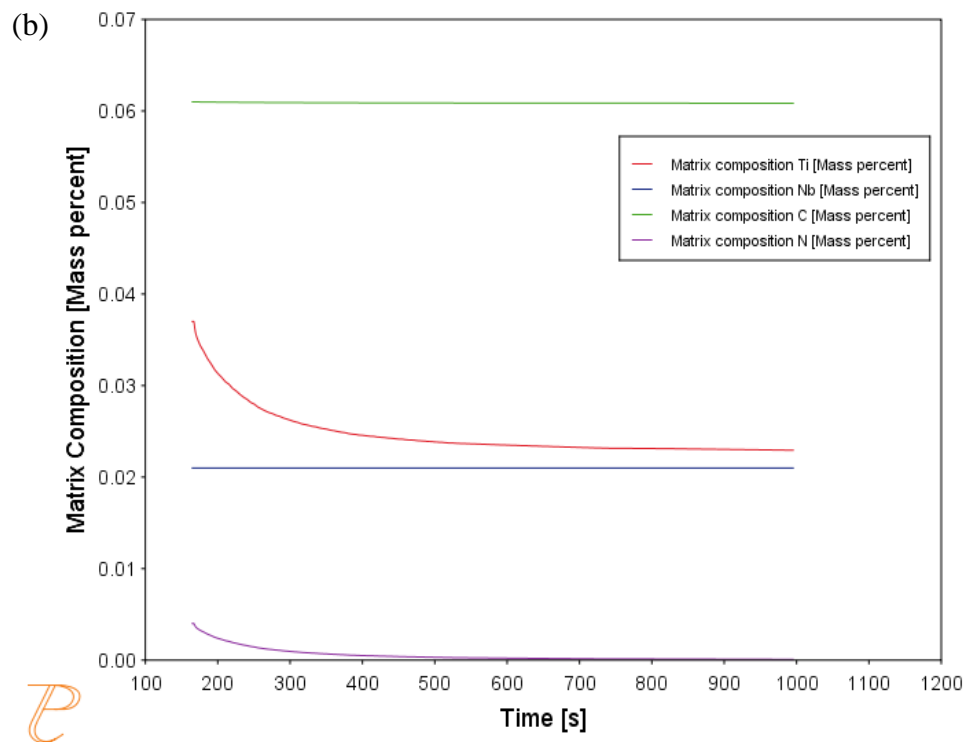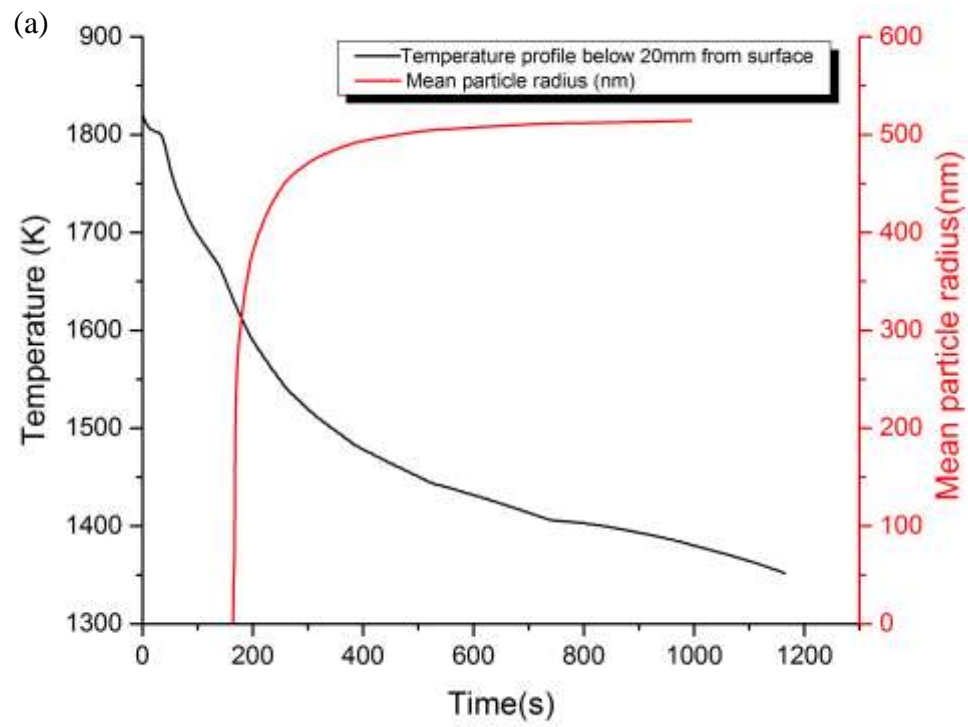
Figure 5.12. Predicted (a) mean particle radius (b) matrix composition at 20 mm below the strand surface
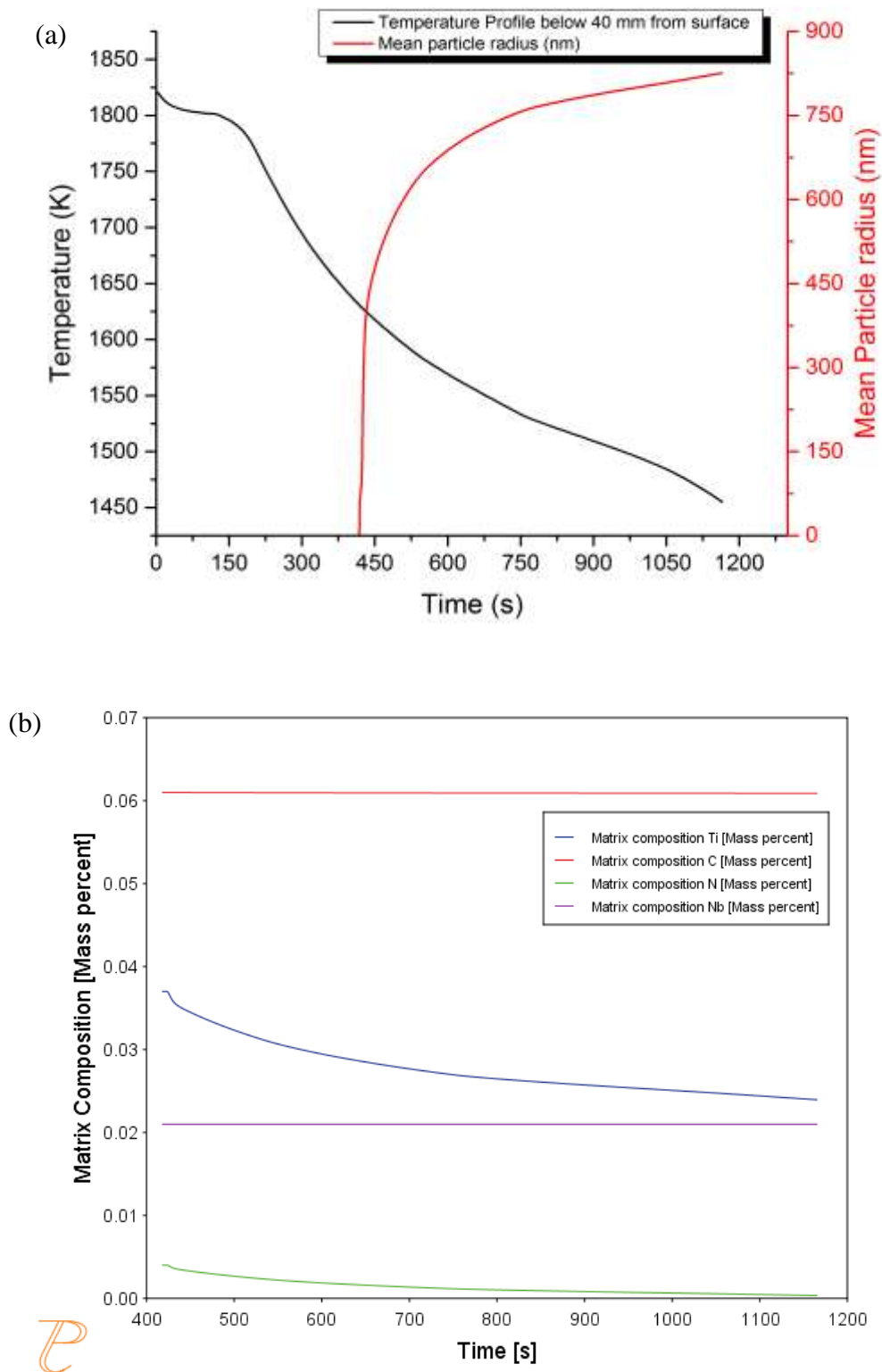
(a)

(b)

Figure 5.13. Predicted (a) mean particle radius (b) matrix composition at 40 mm below the strand surface
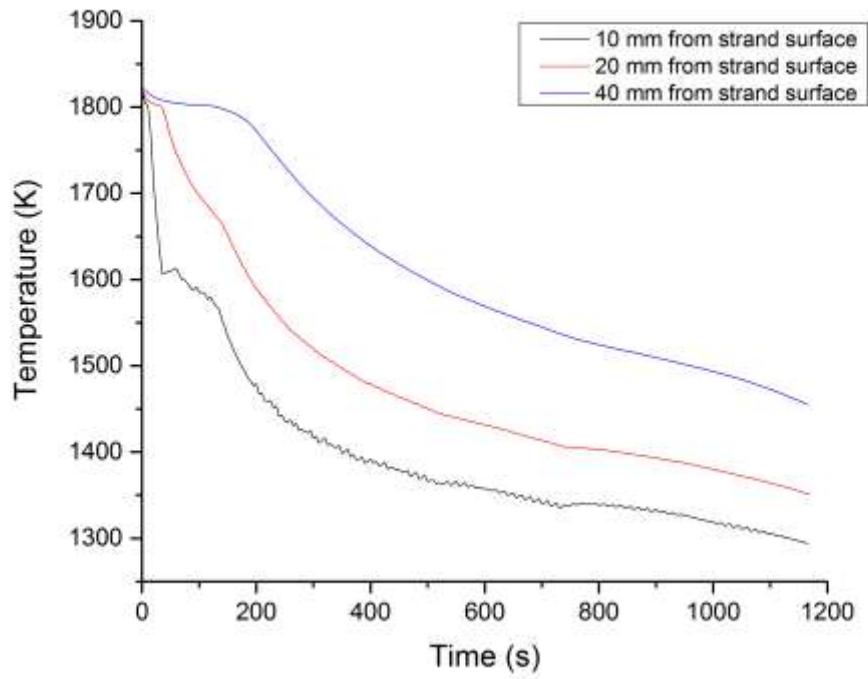
58

Figure 5.14. Predicted temperature history at 10mm, 20mm and 40mm from the strand surface
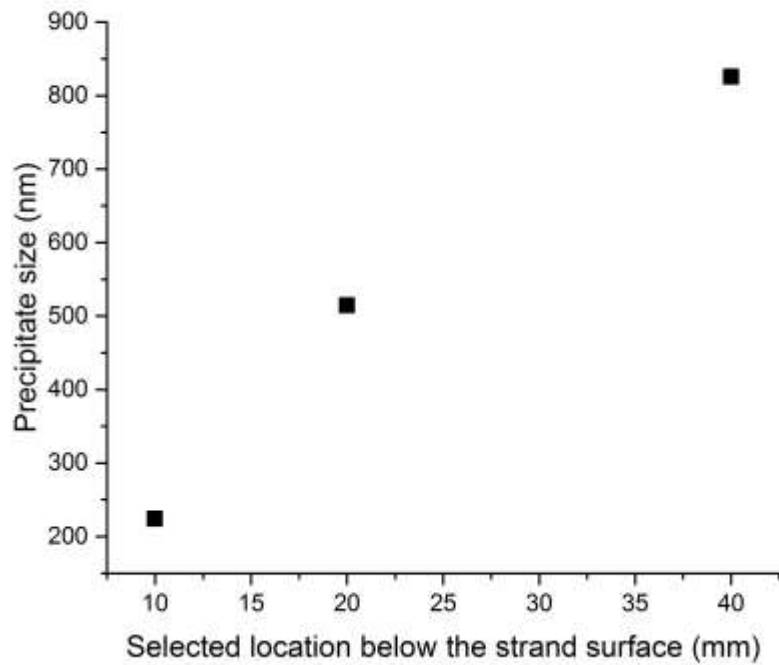

Figure 5.15. Comparison of precipitate size with different location below the strand surface

59

Figure (5.14) and (5.15) shows thermal history and precipitate size at selected locations below the strand surface. From the thermal history, it is observed that the cooling rate is higher at 10mm followed by 20mm and 40mm location from the strand surface. Therefore at 10 mm rate of nucleation is higher than the diffusion rate which leads to decrease in mean particle size. But in 20mm and 40mm locations diffusion rate is dominant which concludes that as distance from the strand surface increases, the cooling rate increases correspondingly the size of precipitate increases.

CHAPTER: 6. Summary

The 1-D transient heat conduction model by enthalpy method for continuous slab caster is developed for micro alloyed steel to predict temperature distribution and shell thickness of the strand. The mathematical model result is compared with CON1D[3] model which shows good agreement. The effect of operation parameters such as casting speed and super heat on temperature distribution and shell growth has been studied. The model can be used as an offline simulation tool for operator guidance

The equilibrium precipitate calculation has been performed by using Thermo-Calc simulation software. The predicted precipitates are $Ti_4C_2S_2$, $Ti(C,N)$, MNS and $(Nb,Ti)C$. In this work $Ti(C,N)$ precipitate has been considered and site fraction of this precipitate has been analysed.

The predicted thermal history from 1-D transient heat conduction model is used for the non-equilibrium precipitation calculation. The precipitation behaviour is studied with help of TC-PRISMA simulation software at three different location of the strand such as 10mm, 20mm and 40mm from the surface and mean particle radius and matrix composition is calculated.

Future Work

- The segregation has not been considered in the present work. Incorporation of this would capture chemical inhomogeneity and the precipitation kinetics can alter accordingly.

- Appropriate experiments need to be conducted (laboratory and plant scale) to validate the model results.

References

[1]   B. G. Thomas, "The Formation of Panel Cracks in Steel Ingots-A State of the art Review," *ISS Trans.*, vol. 7, pp. 7–20, 1986.

[2]   B. G. Thomas, "Modeling of Continuous Casting," *making, Shap. Treat. steel*, pp. 1–24, 2003.

[3]   Y. Meng and B. G. Thomas, "Heat-Transfer and Solidification Model of Continuous Slab Casting: CON1D," *Metall. Mater. Trans. B*, vol. 34B, no. October, pp. 685–705, 2003.

[4]   J. K. Brimacombe, P. K. Agarwal, L. A. Baptista, S. Hibbins, and B. Prabhkar, "Spray Cooling in the Continuous Casting of Steel," in *National Open Hearth and Basic Oxygen Steel Conference*, 1980, pp. 109–123.

[5]   K. J. Schwerdtfeger, "Heat Withdrawal in Continuous Casting of Steel," *Cast. Vol.*, no. d, pp. 1–41, 2003.

[6]   T. Gladman, "*The Physical Metallurgy of microalloyed Steels"*. The Institute of Materials, 1997.

[7]   "Thermo-Calc training." [Online]. Available:
http://www.thermocalc.com/training/training-courses/. [Accessed: 08-Oct-2017].

[8]   E. H. and S. A. Alizedeh M, "Mathematical modeling of heat transfer for steel continuous casting process," *Int J ISSI*, vol. 3, no. 2, pp. 7–16, 2006.

[9]   G. Kaestle, "Heat Flow and Solidification in Strand Coolling ofSlab," *ISS AIME*, vol. 65, 1982.

[10]   T. Kolenko, A. Jaklič, and J. Lamut, "Systems Development of a mathematical model for continuous casting of steel slabs and billets," *ISSN*, vol. 3954, no. 2007, pp. 45–61, 2007.

[11]   A. Maurya and P. K. Jha, "Mathematical Modelling of Solidification in a Curved Strand During Continuous Casting of Steel," *J. Inst. Eng. Ser. C*, vol. 98, no. 1, pp. 45–52, 2017.

[12]   H.-J. Shin, S.-H. Kim, B. G. Thomas, G.-G. Lee, J.-M. Park, and J. Sengupta,

“Measurement and Prediction of Lubrication, Powder Consumption, and Oscillation Mark Profiles in Ultra-low Carbon Steel Slabs,” *ISIJ Int.*, vol. 46, no. 11, pp. 1635–1644, 2006.

[13] M. Gonzalez, M. B. Goldschmit, A. P. Assanelli, E. F. Berdaguer, and E. N. Dvorkin, “Modeling of the Solidi cation Process in a Continuous Casting Installation for Steel Slabs,” vol. 34, no. August, pp. 455–473, 2003.

[14] Ju. Xu, B. G. Thomas, M. S. Dyer, J. G. Speer, and D. K. Matlock, “Model of Microalloy Precipation During Continuous Casting and Reheating,” *Iron Steel Technol.*, no. October, pp. 59–68, 2013.

[15] G. Alvarez de Toledo, A. Arteaga, and J. J. Laraudogoitia, “Continuous Casting of Microalloyed Steels. Influence of Composition and Operational Parameters in Billet Surface Cracking,” *Mater. Sci. Forum*, vol. 500–501, pp. 163–170, 2005.

[16] G. Alvarez de Toledo, A. Arteaga, and J. J. Laraudogoitia, “Continuous Casting of Microalloyed Steels. Influence of Composition and Operational Parameters in Billet Surface Cracking,” *Mater. Sci. Forum*, vol. 500–501, pp. 163–170, 2005.

[17] F. C. Langenberg, J. K. McCauley, and M. C. Dias, “Solidification of Steel,” *Jom*, vol. 15, no. 4, pp. 311–317, 1963.

[18] B. G. Thomas and C. Ojeda, “Ideal taper prediction for slab casting,” *ISSTech Steelmak. Conf.*, pp. 295–308, 2003.

[19] K. A. Taylor, “Solubility products for titanium-, vanadium-, and niobium-carbide in ferrite,” *Scr. Metall. Mater.*, vol. 32, no. 1, pp. 7–12, 1995.

[20] R. C. Sharma, V. K. Lakshmanan, and J. S. Kirkaldy, “Solubility of Niobium Carbide and Niobium Carbonitride in Alloyed Austenite and Ferrite.,” *Metall. Trans. A, Phys. Metall. Mater. Sci.*, vol. 15 A, no. 3, pp. 545–553, 1984.

[21] Zou, “Thermodynamic calculation and experimental verification of the carbonitride austenite equilibirum in Ti Nb microalloyed steels,” vol. 23, no. February, 1992.

[22] Wada and Pehlke, “Nitrogen solubility and nitride formation in austenitic Fe-Ti alloys\t,” *Metall. Mater. Trans. B*, vol. 16B, no. Dec, pp. 815–822, 1985.

[23] K. Schwerdtfeger, “Heat withdrawal in the mold in continuous casting of steel. Review and analysis,” *Steel Res. Int.*, vol. 77, no. 12, pp. 911–920, 2006.